Astronomically-paced changes in paleoproductivity, winnowing, and mineral flux over Broken Ridge (Indian Ocean) since the Early Miocene

J. Lyu[1], G. Auer[2], O.M. Bialik[1], B. Christensen[3], R. Yamaoka[4], D. De Vleeschouwer[1]

[1] Institute of Geology and Palaeontology, University of Münster, Corrensstr. 24, 48149 Münster, Germany

[2] Institute of Earth Sciences (Geology and Paleontology), University of Graz, NAWI Graz Geocenter, Heinrichstraße 26, 8010 Graz, Austria

[3] Department of Environmental Science, School of Earth and Environment, Rowan University, 201 Mullica Hill Rd., NJ 08028, Glassboro, USA

[4] Kochi Institute for Core Sample Research, Japan Agency for Marine-Earth Science and Technology, Japan

Corresponding author: Jing Lyu (j.lyu@uni-muenster.de)

Key Points:

- ODP Site 752 is marked by a 405-kyr and 100-kyr eccentricity and obliquity imprint in XRF-derived records.
- Late Miocene Biogenic Bloom is absent at Broken Ridge according to the XRF-derived paleoproductivity proxy.
- Shift in inter-ocean connectivity to the middle latitudes modified current intensity over Broken Ridge throughout the Miocene.

Abstract

A significant shift in Earth's climate characterizes the Neogene, transitioning from a single-ice-sheet planet to the current bipolar configuration. This climate evolution is closely linked to changing ocean currents, but globally-distributed continuous high-resolution sedimentary records are needed to fully capture this interaction. The Ocean Drilling Program (ODP) Site 752, located on Broken Ridge in the Indian Ocean, provides such a Miocene-to-recent archive. We use X-ray fluorescence (XRF) core scanning to build an eccentricity-tuned age-depth model and reconstruct paleoceanographic changes since 23 Ma. We find two intervals of enhanced productivity, during the early and middle Miocene (18.5 – 13.7 Ma) and late Pliocene/early Pleistocene (3 – 1 Ma). We also report a mixed eccentricity-obliquity imprint in the XRF-derived paleoproductivity proxy. In terms of grain size, three coarsening steps occur between 19.2 – 16 Ma, 10.8 – 8 Ma, and since 2.6 Ma. The steps respectively indicate stronger current winnowing in response to vigorous Antarctic Intermediate Water flow over Broken Ridge in the early Miocene, the first transient onset of Tasman Leakage in the Late Miocene, and the intensification of global oceanic circulation at the Plio-Pleistocene transition. High-resolution iron and manganese series provide a detailed Neogene dust record. This study utilized a single hole from an ODP legacy-site. Nevertheless, we managed to provide novel perspectives on past Indian Ocean responses to astronomical forcing. We conclude that Neogene sediments from Broken Ridge harbor the potential for even more comprehensive reconstructions. Realizing this potential necessitates re-drilling of these sedimentary archives utilizing modern drilling strategies.

Plain Language Summary

This study looks into how the Indian Ocean changed since the start of the Neogene (last 23 million years). We use X-ray fluorescence (XRF) analyses to measure the chemical composition of a marine sediment core (ODP Site 752), drilled on Broken Ridge at 1086 m water depth. Our results show that the central Indian Ocean had overall higher productivity levels between 18.5 – 13.7 million years ago, but productivity levels varied significantly on timescales from ten thousand to hundred thousand years. These changes were influenced by variations in the Earth's orbit around the Sun. The grain size of the sediment became coarser at three intervals during the last 23 million years, which is thought to be caused by stronger ocean currents over Broken Ridge at those times. Overall, the study suggests that the Indian Ocean has gone through significant changes in the past and that the sediment from this site could be useful for further paleoceanographic research.

1 Introduction

The global ocean is an interconnected system, regulating the atmosphere, climate and elemental budgets (e.g., Broeker, 1991, Stocker et al., 1992). The Indian Ocean acts as a switchboard within this system, connecting the larger water masses of the Pacific and the Atlantic Oceans. Today, direct connectivity between the larger ocean basins is mainly exclusive to the middle latitudes. But, in the past, low-latitude inter-basin connections played a more significant role. As the Indian Ocean transitioned from an open tectonic configuration to a restricted configuration throughout the Neogene, it underwent significant changes in its climatic and oceanic organization. Two major oceanic gateway closures affected Indian Ocean connectivity during the Neogene. The first was the restriction of the Indonesian Gateway (between Borneo and New Guinea, ~25 Ma, Kuhnt et al., 2004), which connects the Pacific to the Indian Ocean. This restriction blocked the flow of warm Pacific water into the Indian Ocean (Kuhnt et al., 2004). The second was the final termination of the Tethyan Ocean (~13.8 Ma, Bialik et al., 2019). This final closure of the Tethyan Ocean decoupled the Mediterranean Sea and the Indian Ocean, preventing Indian Ocean warm water from flowing west and entering the Atlantic Ocean at low latitudes. The closure of the Tethys shifted the inter-basinal connection between the Indian and Atlantic oceans to the mid-latitudes. Hence, surface waters were forced south around Africa (Agulhas Leakage; de Ruijter et al., 1999; Durgadoo et al., 2017; Gordon, 2003; Ohishi et al., 2017; Ridgway & Dunn, 2007). This configuration is marked by three inter-connected southern subtropical gyres, which together form the Southern Hemisphere Supergyre (Speich et al., 2002; Ridgway & Dunn, 2007). To a lesser extent, similar shift occurred between the Pacific and Indian oceans. The link between the Pacific and Indian oceans occurs mainly through routes the low-latitude Indonesian Throughflow (ITF, Gordon et al., 2005) and the

middle-latitude Tasman Leakage (TL, Speich et al., 2001). The ITF transports water from the Pacific to the Indian Ocean at surface water depths (<300 m, van Sebille et al., 2014). Tasman Leakage occurs at intermediate water depths south of Australia (Middleton, 2002, Speich et al., 2002, van Sebille et al., 2012, 2014, Rosell-Fieschi et al., 2013) and was established ~7 Myr ago (Christensen et al., 2021) – marking another connectivity shift to the middle-latitudes.

Neogene shifts in Indian Ocean dynamics are also interwoven with the evolution of the monsoon systems. Monsoonal winds drive ocean currents and contribute to upwelling and downwelling (Betzler et al., 2016, Bialik et al., 2020). Hence, monsoonal winds influence ocean salinity, temperature, oxygen, and nutrient levels. Previous research (Dickens & Owen, 1994) has suggested the existence of an expanded oxygen minimum zone (OMZ) between 6.5 to 3 Ma, ranging from the northern Indian Ocean as far south as Broken Ridge. This interpretation is mainly based on observations of Mn depletions at Broken Ridge and benthic foraminifera assemblages (Dickens & Owen, 1994, Gupta et al., 2013). However, the timing and extent of this OMZ during the Late Miocene are poorly understood. Definitive evidence for the cross-hemispheric expansion of the Indian Ocean OMZ is currently lacking.

Over the last decade, the International Ocean Discovery Program (IODP) has primarily focused on the Indian Ocean marginal areas, particularly on regions influenced by monsoons (Clift et al., 2022). However, locations in the interior of the Indian Ocean also holds great potential for revealing shifts in the position of the Indian Ocean gyres, productivity patterns, and general changes in ocean circulation. Such regions were sampled by the Ocean Drilling Program (ODP) in the 1980's and 90's. For example, ODP Leg 121 drilled Site 752 on Broken Ridge. Broken Ridge is a west-northwest trending oceanic plateau in the central Indian Ocean that separated from the Kerguelen Plateau during the middle Eocene (~42 Ma). Since then, it has

drifted from a ~55°S paleolatitude to its present-day location at ~31°S (Berggren et al., 1985; Mutter & Cande, 1983). It was accompanied with subsidence but no large-scale tilting during its northward drift. This makes for a ~100 m-thick package of Neogene sediments that accumulated on Broken Ridge. At ODP Site 752, this so-called horizontal cap consists of nannofossils ooze with foraminiferal sand (94.5 – 97% $CaCO_3$, Peirce & Weissel, 1989). While Site 752 has good recovery in its Neogene section (~95.9%), the site has not yet been studied for paleoceanography on astronomical timescales. Moreover, due to its location and the intermediate water depth, this site can be used for tracing Antarctic Intermediate water (AAIW), and Tasman Leakage (TL). Nevertheless, this sedimentary archive has the potential to reveal spatial and temporal changes in Indian Ocean paleoceanography since the Early Miocene. This is mainly because new techniques, like cm-scale X-Ray Fluorescence (XRF) core scanning, are standardly used nowadays but were not yet available at the time of coring.

In this study, we generate an astronomically-tuned age-depth model, based on the XRF-derived calcium-iron (Ca/Fe) ratios downcore. Thereby, it is important to acknowledge that the XRF data used in this study originate from a single hole (ODP Hole 752A), precluding the application of stratigraphic splicing techniques employed in contemporary IODP paleoceanographic studies. Nonetheless, the 95.9%-recovery achieved in Hole 752A enables us to develop an age-depth model based on the eccentricity scale. This age-depth model is then used to investigate time-series of other elemental proxies and to characterize oceanographic change at Broken Ridge since the Early Miocene (e.g., productivity, current winnowing, and dust transport).

121 ## 2 Materials and Methods

122 ### 2.1 Site description

123 Ocean Drilling Program (ODP) Hole 752A (Fig. 1a) was drilled near the crest of Broken
124 Ridge (30°53.475'S, 93°34.652'E; 1086.3m water depth). Broken Ridge separated from the
125 Kerguelen Plateau due to lithospheric extension and seafloor spreading that began before 42 Ma
126 (Berggren et al., 1985; Mutter & Cande, 1983). Broken Ridge has moved north by about 20° of
127 latitude since the Middle Eocene as part of the Indo-Australian plate. More than 1500 m of
128 sediments have accumulated on Broken Ridge, recording the oceanographic history of the Indian
129 Ocean from the Late Cretaceous until today. Sediments from Broken Ridge consist of four major
130 sections. The horizontal cap (fourth section) has been recovered at Site 752, 753, 754, 755 and
131 1141 (Peirce & Weissel, 1989, Coffin et al., 2000). At Site 752, the horizontal cap consists of
132 nannofossils and foraminiferal ooze with foraminiferal sand (94.5 – 97% $CaCO_3$). The base of
133 the horizontal cap includes some upper Eocene and upper Oligocene sediments, but it chiefly
134 consists of Neogene carbonate oozes, deposited under pelagic conditions (Peirce & Weissel,
135 1989). For this study, we exclusively focus on the Neogene portion of the horizontal cap, clearly
136 above the angular unconformity, studying sediments between cores 752A-1H and 752A-10H (0
137 – 91.70 meters below sea floor (mbsf); Fig. 1b).

138 Broken Ridge has always been located in intermediate water depths throughout the studied
139 interval. The angular unconformity described above consists of two pebble layers at the bottom
140 of the horizontal cap. Subsequent paleo-water depths gradually deepen up section. Sclater et al.
141 (1985) calculated 316 m of subsidence for Broken Ridge since 22 Ma, based on an assumption
142 that the Broken Ridge crust is 85 Myr old. However, the age of the crust is ~100 Ma according to

the shipboard scientific party (Peirce & Weissel, 1989). For that reason, we assume that Neogene subsidence rates at Broken Ridge must have been less than 316 m over the last 22 Myr. Moreover, the paleo-water-depth reconstruction from benthic foraminifera suggests that water depths were already as deep as ~800 m water around 23 Ma, with only a slight and gradual deepening afterwards, to around a water depth of ~1000 m today (Driscoll et al. 1991). Paleobathymetric records by Peirce & Weissel (1989) also corroborate that Site 752 has remained at intermediate water depths throughout the Neogene.

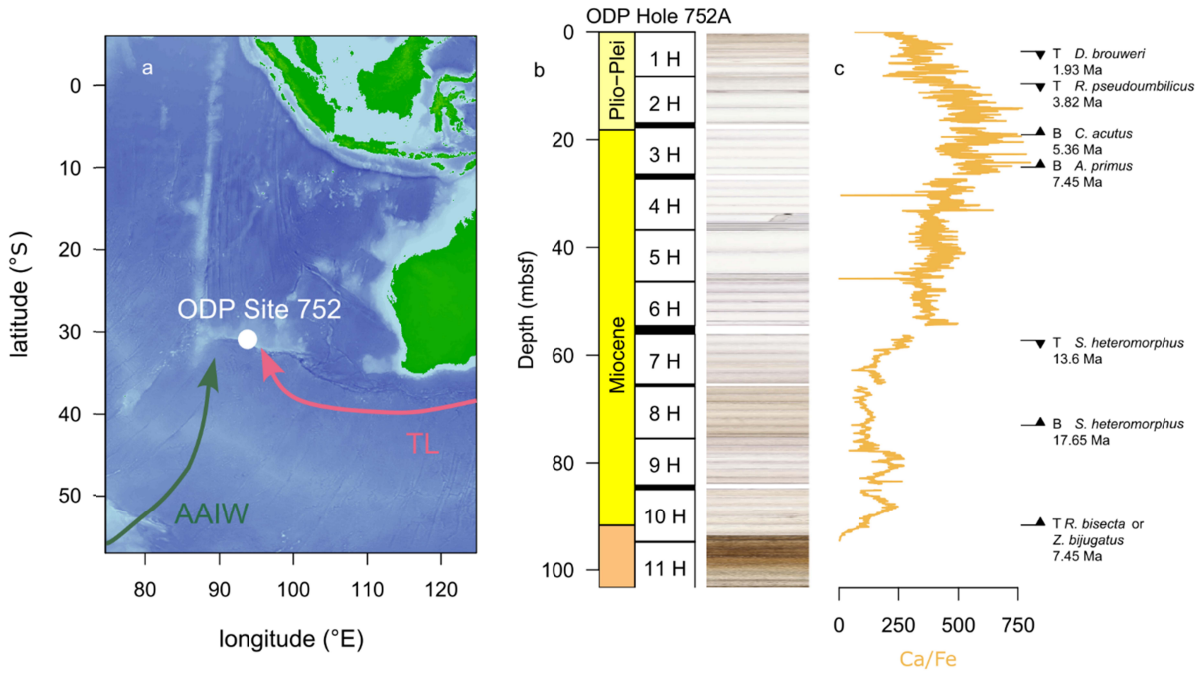

Figure 1. Geologic setting. (a) Location of ODP Site 752 drilled at 1086.3 m water depth on the Broken Ridge, central Indian Ocean. TL = Tasman Leakage (pink arrow), AAIW = Antarctic Intermediate Water (green arrow). Bathymetry is from Earth TOPOgraphy 1 (ETOPO1) (Amante & Eakins, 2009); **(b)** Core recovery at ODP Hole 752A **(**Cores 1H - 11H) with core photographs; **(c)** XRF-derived Ca/Fe ratios (unitless), and biostratigraphy. T = top, B = base.

2.2 X-ray fluorescence core scanning

The bulk elemental composition of ODP Hole 752A sediments was measured on the archive-half core surfaces using X-ray fluorescence core scanning using an Itrax XRF scanner (Löwemark et al., 2019) at the Kochi Core Center, Kochi, Japan. Measurements were taken at a spatial resolution of 2 cm, with an X-Ray beam size of 0.2 x 20 mm, a Molybdenum X-Ray source energy of 30 kV (55 mA, no filter), and a 10 s count time for each measurement. Element intensities (in counts) were obtained by processing raw X-ray spectra using the ITRAX software for the elements Al, Si, P, S, Cl, Ar, K, Ca, Ti, V,Cr, Mn, Fe, Ni, Cu, Zn, Ga, As, Se, Br, Rb, Sr, Y, Zr, Cd, Sn, Cs, Ba, Ta, W, Re as well as the coherent (coh) incoherent (inc) scatter of the Molybdenum X-ray source.

2.2.1 Paleoproductivity index

To reconstruct changes in paleoproductivity, we utilize a group of metallic micronutrients (Cd, Cu, Ni, Zn, Cr and Br). These elements are usually depleted at the surface ocean by biology, we argue their accumulation in the sediment could be used to trace productivity (Tribovillard et al., 2006, Steiner et al., 2017). To generate a paleoproductivity index we summed up the XRF counts of all productivity-related elements and multiplied by 1000. To account for the background, we then divided the product by Ca counts. This paleoproductivity index is designed to capture fluctuations in the relative strength of the nutrient-limited biological pump versus the alkalinity pump.

We recognize that counts for the selected metallic micronutrients are generally low. Nevertheless, we argue that each of those elements carries a paleoproductivitiy signal (and is therefore not pure noise) because of three main reasons. First, for all these elements, an exposure

178 time of 10 s is sufficient to obtain reliable results according to the practical guidelines in
179 Löwemark et al. (2019). Second, the covariance matrix (Fig. S1) of Cd/Ca, Cu/Ca, Ni/Ca, Zn/Ca,
180 Cr/Ca and Br/Ca shows that these productivity-related elements are mostly positively correlated,
181 and hence likely to be reflecting the same paleoproductivity signal. Especially Zn, Cr, Ni and Cu
182 seem to be elements with mutually consistent (and therefore non-random) signals. Third, and
183 most importantly, our paleoproductivity index exhibits co-variation with shipboard C_{org}
184 measurements.

185 2.2.2 Current winnowing proxy

186 Here, we use the total counts received by the XRF core-scanner detector as a measure of
187 sediment bulk density. Total counts record shows a good agreement with the shipboard GRA
188 bulk density (Fig. S2), which supports that total counts record relates to the sediment bulk
189 density and can be used as proxy for the current winnowing. We also checked the
190 paleoproductivity index with this XRF-derived current winnowing proxy, which show no
191 correlation between these two records.

192 2.3 Grain size analysis

193 Grain size measurements of 123 samples throughout the last 23 million years were
194 conducted in the Particle-Size Laboratory at MARUM, University of Bremen with a Beckman
195 Coulter Laser Diffraction Particle Size Analyzer LS 13320. Samples were first diluted (dilution
196 factor: >25), and the samples were boiled with ~0.3 g tetra-sodium diphosphate decahydrate
197 ($Na_4P_2O_7 * 10H_2O$) to ensure fully disaggregated prior to the measurements (McGregor et al.,
198 2009). All preparation steps and measurements were carried out with deionized, degassed and
199 filtered water (filter mesh size: 0.2 μm) to reduce the potential influence of gas bubbles or

particles within the water. The particle-size distribution result of a sample consists of 116 size classes (from 0.04 to 2000 µm). The calculation of the particle sizes relies on the Fraunhofer diffraction theory and the Polarization Intensity Differential Scattering (PIDS) for particles from 0.4 to 2000 µm and from 0.04 to 0.4 µm, respectively. The reproducibility was checked regularly when analyzing the full sample by replicate analyses of three internal glass-bead standards and is found to be better than ±0.7 µm for the mean and ±0.6 µm for the median particle size (1σ). The average standard deviation integrated overall size classes is better than ±4 vol% (note that the standard deviation of the individual size classes is not distributed uniformly). All provided statistic values are based on a geometric statistic.

2.4 Biostratigraphy

Biostratigraphic age control points from the shipboard report (Peirce & Weissel, 1989) were updated to GTS2020 (Table 1, Raffi et al., 2020). During the expedition, 4-to-5 cm thick biostratigraphic samples were taken from every core catcher (i.e., every ~9 m). The depth error shown in Table 1 was calculated by taking the stratigraphic distance between the proposed stratigraphic depth of the datum in the shipboard report and the stratigraphic depth of the corresponding biostratigraphic sample. The biostratigraphic age-depth tie-points (Table 1) suggest relatively stable sedimentation rates throughout the studied interval, ranging between 2.9 and 5.7 m/Myr.

Table 1. Calcareous nannofossil datums (Peirce & Weissel, 1989) used for depth-age correlation at ODP Hole 752A. Samples for biostratigraphy have been taken from every core-

221 catcher in the studied interval between cores 752A-1H and 752A-10H. We estimate the depth
222 error by reporting the stratigraphic distance between the datum and the corresponding sample.

Datum T = Top, B = Base		References	Depth (mbsf)	Depth error (mbsf)	Age (Ma, from GTS2020)
T	*Discoaster brouweri*	Curry et al. (1995)	4.3	±3.96	1.93
T	*Reticulofenestra pseudoumbilicus*	Curry et al. (1995)	10.3	±2.04	3.82
B	*Ceratolithus acutus*	Backman and Raffi (1997);	19.1	±2.23	5.36
B	*Amaurolithus primus*	Raffi and Flores (1995)	25.1	±1.31	7.45
T	*Sphenolithus heteromorphus*	Backman and Raffi (1997)	58.1	±3.57	13.6
B	*Sphenolithus heteromorphus*	Backman et al. (2012)	73.1	±2.4	17.65
T	*Reticulofenestra bisecta* or *Zygrhablithus bijugatus*	Roth, 1970, Deflandre 1959	91.7	±3.17	23.04

223

224 2.5 Time-series analysis

225 Spectral analyses in this study were carried out using the multitaper method (MTM) with
226 five 2π-tapers (Thomson, 1982) and robust AR(1) background estimation (Meyers, 2012), as
227 implemented in the R-package *astrochron* (Meyers, 2014). We emphasize that the analyzed XRF
228 dataset originates from a single hole is characterized by up to 1.92-m-long datagaps in-between

229 cores 752A-6H and 752A-7H. In present-day paleoceanographic studies, this issue is alleviated
230 by constructing a stratigraphic splice using multiple holes. To better illustrate the effect of these
231 datagaps, and to account for possible changes in sedimentation rate, we also carry out wavelet-
232 transform time-series analysis. Wavelet analysis was conducted using R-package biwavelet
233 (Gouhier et al., 2021). Depth-to-time conversion and bandpass filtering were carried out using
234 functions “tune” and “bandpass” from the R-package *astrochron*.

3 Astrochronology

We adopt an astrochronologic approach to reconstruct the age-depth model (Table 1). First, we detrended the Ca/Fe depth series by cutting off the frequency smaller than 0.05 cycles/m, and apply wavelet and spectral analysis to the Ca/Fe series in the depth domain. The power spectrum of the Ca/Fe depth series (Fig. 2b) shows a spectral peak ~0.63 cycles/m (~1.6 m/cycle), which may reflect the imprint of the long 405-kyr eccentricity cycle given the biostratigraphic estimate of long-term average sedimentation rate around 5.7 m/Myr. We suspect that Ca/Fe is climatically controlled by aridity, which in turn could have driven changes in eolian flux. The same periodicity can be discerned from the wavelet transform, at least between 0 – 33 mbsf and 44 – 65 mbsf (white dashed line on Fig. 3a). While the MTM power spectrum does not show a spectral peak that could be associated with 100-kyr eccentricity, the wavelet spectrum exhibits a bifurcation pattern at ~0.4 m cycles, and markedly higher periodicities between 33 – 44 mbsf (white circles on Fig. 3a). The bifurcation pattern is in an agreement with the long-eccentricity amplitude modulation of the 100-kyr cycles. The wavelet analysis thus suggests relatively stable sedimentation rates, in agreement with the biostratigraphic estimate, except for the interval between 33 – 44 mbsf, where sedimentation rates might have been somewhat higher. The wavelet transform also suggests significant variability at periodicities in-between the interpreted 100-kyr and 405-kyr eccentricity bands. This spectral power could tentatively be ascribed to the 173-kyr term in obliquity amplitude modulation.

In a next step, a broad Gaussian bandpass filter is applied to the Ca/Fe series. The filter is centered on the peak at ~0.63 cycles/m (bandwidth: 0.4 – 0.95 cycles/m). We fine-tuned the XRF- derived Ca/Fe series according to the above-described astronomical interpretation by correlating maxima in the Ca/Fe ~0.63 cycles/m filter to eccentricity maxima and vice versa

(grey connecting lines between Figs. 3a and 3b). This strategy can be adopted between 0 and 15.1 Ma, but the older interval (15.1 – 23.0 Ma) does not exhibit the clear ~405-kyr imprint needed for astronomical tuning. Therefore, we use the biostratigraphic tie-points in the >15.1 Ma interval. We do not include any phase-lags while tuning. The phase relationship between the proxy and the astronomical solution is in agreement with the findings by Vervoort et al. (2021) for pelagic carbonates. This phase-relationship implies that more arid climates around the Indian Ocean correspond to eccentricity minima (e.g., De Vleeschouwer et al., 2018, Duesing et al., 2021, Liu et al., 2021). The power spectrum (Fig. 2c) of the astronomically-tuned Ca/Fe time-series shows an obliquity signal, reaching to the 99% confidence level. We present the Ca/Fe time-series along the final astronomically-tuned age model in Fig. 3d.

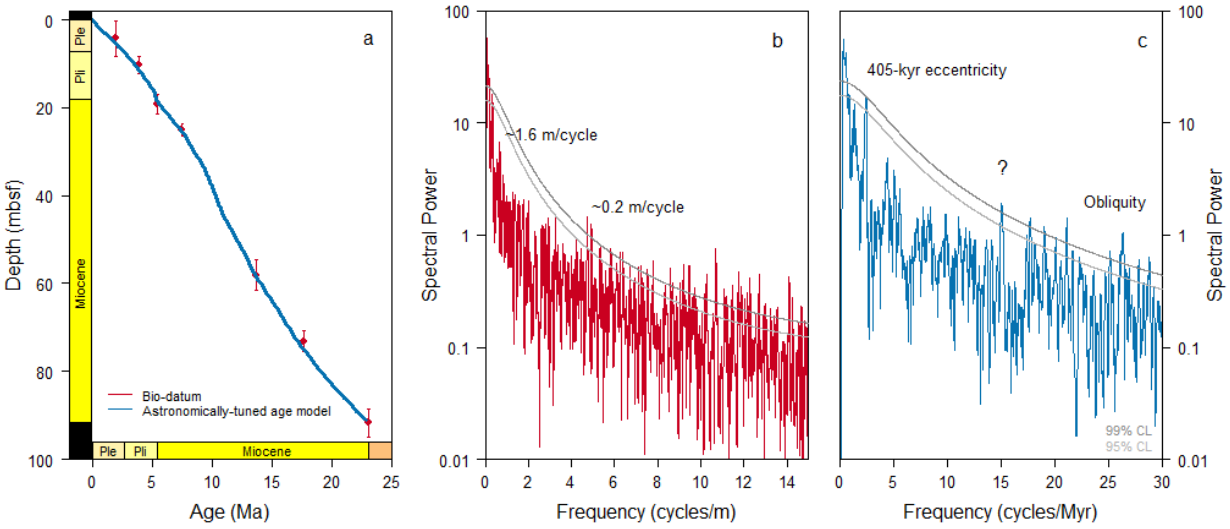

Figure 2. Spectral analysis of Ca/Fe series. (a) Spectral power distribution of the Ca/Fe time-series along the biostratigraphic datums (red dots) with error bars showing depth-uncertainties and the astronomically-tuned age model (blue); **(b)** Spectral power distribution of the Ca/Fe depth-series. The grey line represents the 99% of confidence interval and the light grey line represents the 95% of confidence interval; **(c)** Spectral power distribution of the Ca/Fe time-series along the astronomically-tuned age model. The grey line represents the 99% of confidence interval and the light grey line represents the 95% of confidence interval.

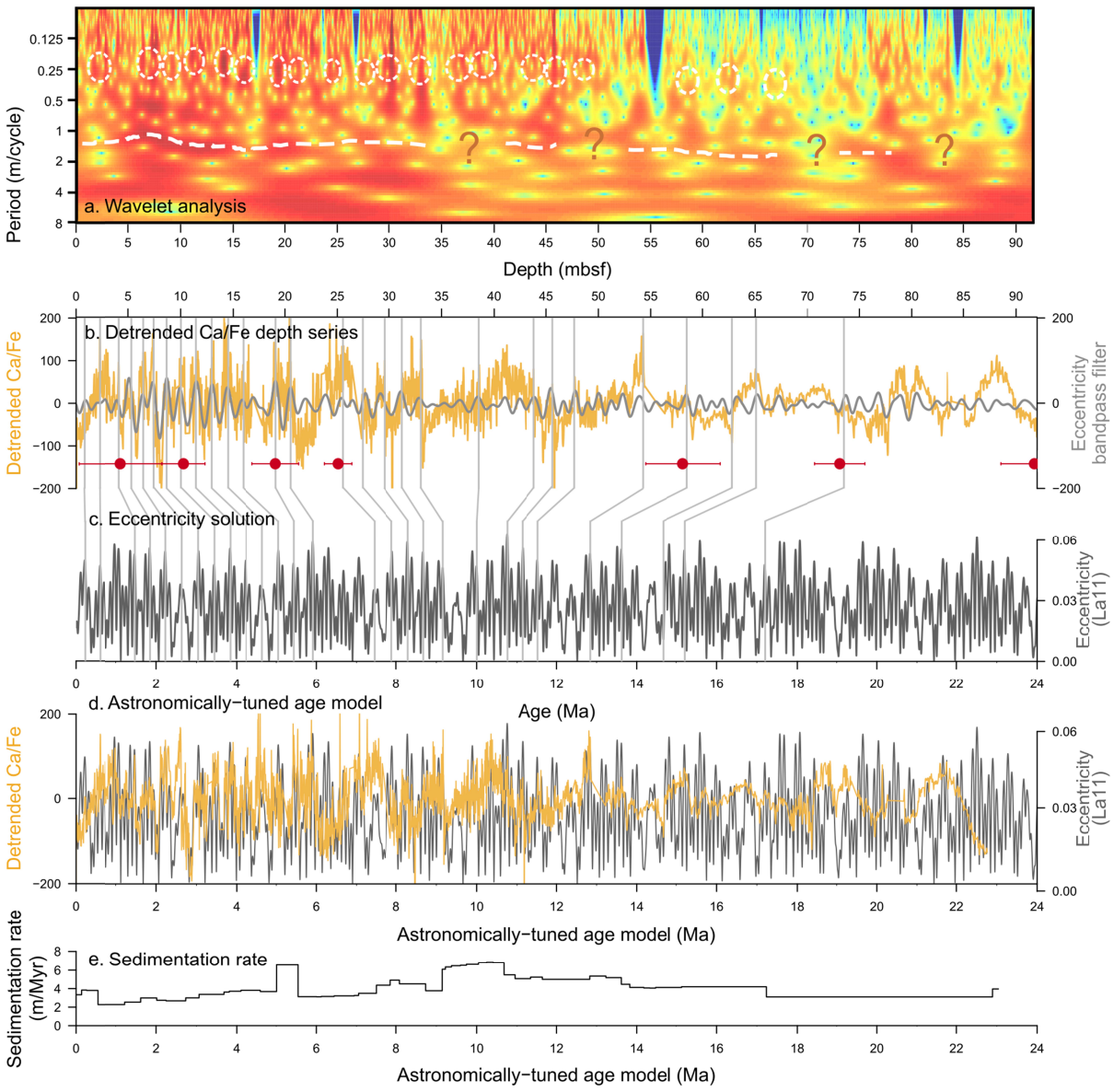

278

279 **Figure 3. Astrochronology. (a)** Wavelet analysis of detrended Ca/Fe depth-series. The dash line
280 indicates the power at ~1.6 m/cycle, while the circles indicate the power at ~0.2 m /cycle. **(b)**
281 Detrended Ca/Fe depth-series (yellow) and its ~1.6 m/cycle filter (gray), and red dots represent
282 the stratigraphic position of biostratigraphic datum; **(c)** La11 Eccentricity solution as a tuning
283 target; **(d)** Detrended Ca/Fe time-series according to the astronomically-tuned age-depth model

(yellow) and La11 Eccentricity solution (gray). The astronomically-tuned age-depth model is refined by tuning maxima in Ca/Fe depth series into eccentricity maxima; **(e)** Sedimentation rate.

4 Elemental geochemistry

The XRF-derived elemental geochemistry dataset generated for ODP Hole 752A consists of 31 elements, of which several have the potential to serve as a proxy for specific environmental parameters (Löwemark et al., 2019). In the following subsections, we will discuss the XRF-derived elements according to their environmental interpretation.

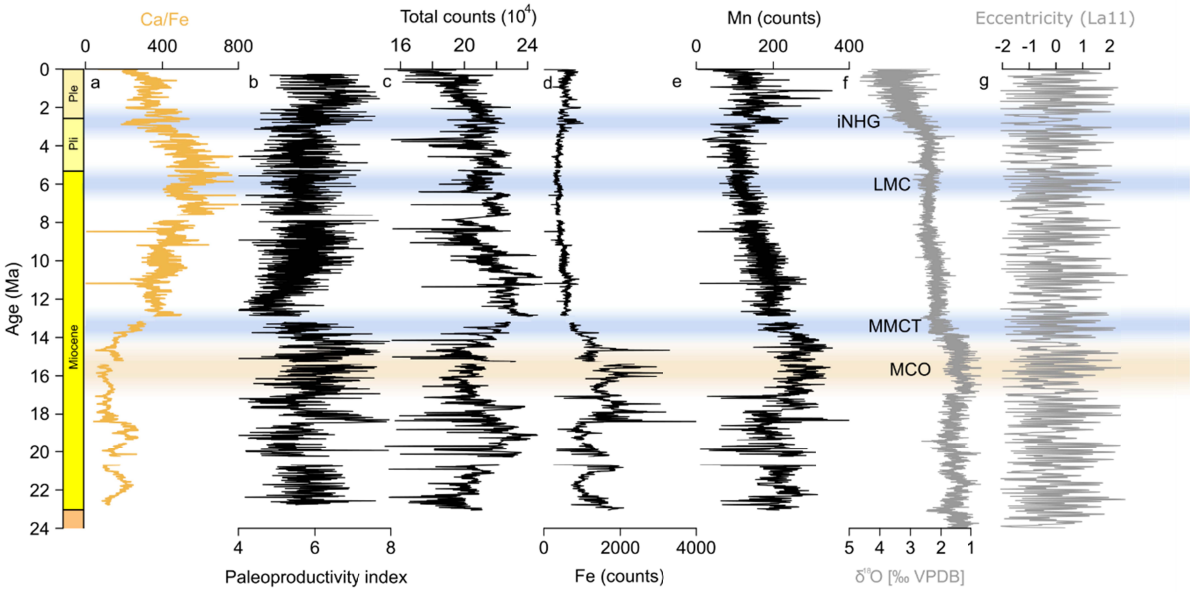

Figure 4. XRF elements plot. (a) XRF-derived Ca/Fe ratio as a proxy for carbonate content and used for astrochronology (unitless). **(b)** Paleoproductivity proxy (paleoproductivity index = 1000*(Cd+Cu+Ni+Zn+Cr+Br)/Ca; unitless); **(c)** Total counts received by the XRF detector is dependent on sediment bulk density, which -in this case- serves as a proxy for current winnowing; **(d)** Fe counts; **(e)** Mn counts; **(f)** Benthic foraminiferal $\delta^{18}O$ megasplice (De Vleeschouwer et al., 2017); and **(g)** La11 eccentricity solution. All data are plotted on the astronomically-tuned age model. MCO: Miocene climatic optimum; MMCT: Middle Miocene

climate transition; LMC: Late Miocene cooling; iNHG: intensification of Northern Hemisphere glaciation.

4.1 Paleoproductivity

The paleoproductivity index fluctuates at relatively high values in the Early and Middle Miocene before sharply decreasing around 14 Ma (Fig. 5a). This pattern shows the same trend as the low-resolution shipboard record of organic carbon content (Peirce & Weissel, 1989, Fig. 5a), which again, approved the validation of this paleoproductivity proxy. The index rebounds after the middle Miocene minimum and then maintains a rather stable level until the Late Pliocene. None of these shifts correspond to the Late Miocene-Early Pliocene Biogenic Bloom event in the Indian Ocean and elsewhere (Dickens & Owen, 1999, Hermoyian & Owen, 2001, Grant & Dickens, 2002, Karatsolis et al., 2022). Nor do we observe particularly elevated productivity levels around the time of the biogenic bloom (Fig. 5a, b). This is consistent with the very heterogeneous nature of the Late Miocene Biogenic bloom (Pillot et al., 2023): The Biogenic Bloom appears to have been highly magnified in already high productivity zones, whereas ODP Site 752 was located in the center of a low productivity oceanic gyre throughout the studied interval. ODP Site 752 is also far away from any continental margin area or upwelling zone. All these factors combined make ODP Site 752 less suited to capture the surface productivity increase of the biogenic bloom.

The multitaper power spectrum of the paleoproductivity index displays statistically-significant peaks at frequencies that are reminiscent of 405-kyr and ~100-kyr eccentricity forcing. Elevated spectral power can also be observed at higher frequencies, possibly hinting at an imprint of obliquity and precession (Fig. 6). However, the 2-cm sampling resolution (~5 kyr

temporal resolution) may not be adequate to interpret the highest-frequency peaks (precession) with confidence. We interpret the paleoproductivity reconstruction to be driven by eccentricity and obliquity on astronomical timescales. Therewith, we make a similar inference as Karatsolis et al. (2022), who constructed and analyzed a low-latitude global paleoproductivity composite between 7 and 3 Ma. Our Broken Ridge paleoproductivity reconstruction shows similar dynamics to the Karatsolis record on eccentricity timescales before 4.4 Ma. Following 4.4 Ma, however, the behavior diverges (Fig. 5b). Karatsolis et al. (2022) report a sudden collapse of paleoproductivity (inferred to be the end of the Biogenic Bloom) at 4.4 Ma, whereas paleoproductivity levels at Site 752 remain unchanged before and after 4.4 Ma. The divergence between the two records reiterates the fact that Site 752 lies outside any of the oceanic productivity belts, and therefore exhibits an independent paleoproductivity signal. This signal is influenced by the same orbital parameters (eccentricity and obliquity) – but is not impacted by the large-scale shifts in nutrient availability occurring at oceanic margins. It would also suggest that the productivity gradients between oceanic margins and Broken Ridge during the Biogenic Bloom may have been steeper.

We suggest that the paleoproductivity patterns as recorded by ODP Hole 752A were primarily influenced by the northward tectonic movement of the Broken Ridge plateau, climate-driven changes in the latitude of the subtropical front, and astronomically-paced changes in global ocean circulation. During the Early and Middle Miocene, Broken Ridge was situated at a latitude of ~40°S and we find enhanced paleoproductivity during globally-warm eccentricity maxima. This phase-relationship is illustrated by the negative correlation between our productivity index and the benthic foraminiferal $\delta^{18}O$ record (note the flipped isotope axis in Fig. 5c). This observation is in an agreement with the eccentricity-pacing of ocean, climate and

346 carbon cycle dynamics in the Middle Miocene, as described in Holbourn et al. (2007). At that
347 time, low eccentricity orbits might have favored organic carbon burial and global cooling.
348 Eccentricity maxima on the other hand, especially precession-driven maxima in austral summer
349 insolation, resulted in a smaller Antarctic ice sheet (De Vleeschouwer et al., 2017). With a
350 warmer planet and smaller ice sheet came less vigorous ocean circulation, lower calcium
351 carbonate saturation states in the ocean and a net flux of CO_2 from the ocean to the atmosphere.
352 These warmer conditions have also been inferred to be associated with more intense monsoons
353 (Holbourn et al., 2007). For ODP Hole 752A, we infer a higher paleoproductivity index during
354 eccentricity maxima (Fig. 4b, g), suggesting a simultaneous enhancement of the biological pump
355 and possibly a less efficient alkalinity pump. This model is best illustrated by the rapid rise in
356 paleoproductivity index after 18.5 Ma (Fig. 5a): This interval coincides with a rapid increase in
357 eccentricity forcing after a long-term 2.4-Myr eccentricity minimum (Fig. 4b, g) and a rapid
358 warming after one of the coolest intervals of the Early-Middle Miocene (Holbourn et al., 2015).

359 The globally-warm period of the Early and especially the Middle Miocene (Miocene
360 Climatic Optimum, MCO) was abruptly terminated by a major increase in Antarctic ice volume
361 and a global sea level fall at 13.9 Ma. This global cooling (Middle Miocene Climatic Transition,
362 MMCT) coincided with a dramatic decline of productivity over Broken Ridge. This event is
363 paired with a rapid rise and fall in oceanic turnover (Crampton et al., 2016). Afterwards,
364 productivity slightly recovered and remained rather stable throughout the Late Miocene and early
365 Pliocene. This stability is likely the result of the northward tectonic movement of Broken Ridge
366 on the one hand, and the simultaneous northward shift of the Southern Hemisphere climate belts
367 on the other hand (Groeneveld et al., 2017). Throughout this interval, Broken Ridge was
368 probably situated slightly north of the subtropical front. The most recent increase in

369 paleoproductivity occurs around 3.5 Ma and coincides with generally cool climate conditions
370 across the Southern Hemisphere and a more northerly position of the subtropical front (De
371 Vleeschouwer et al., 2022). This shift in the latitudinal position of the climate belts leads to a
372 contraction of the Indian Ocean gyre, and positioned the subtropical front north of Broken Ridge.
373 Thus, Broken Ridge would be closer to the higher-productivity area, which is outside of the
374 oligotrophic Indian Ocean gyre.

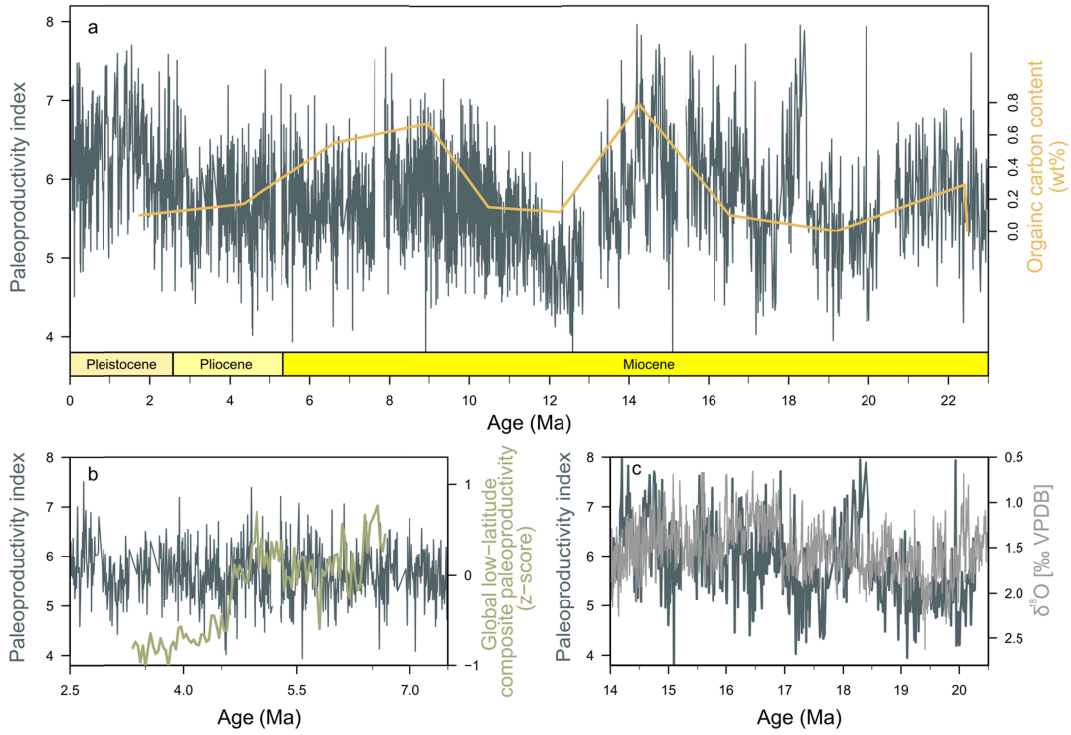

375

376 **Figure 5. Paleoproductivity. (a)** Paleoproductivity index (dark green) calculated for ODP Hole
377 752A since the early Miocene (1000*(Cd+Cu+Ni+Zn+Cr+Br)/Ca) with the shipboard organic
378 carbon content record (gold, Peirce & Weissel, 1989); **(b)** ODP Hole 752A paleoproductivity
379 index (dark green) compared to paleoproductivity composite by Karatsolis et al. (2022) (light

380 green) from 8 to 2 Ma; **(c)** ODP Hole 752A paleoproductivity index (dark green) compared to
381 the benthic $\delta^{18}O$ megasplice (De Vleeschouwer et al., 2017) (grey) from 20.5 to 14 Ma.
382

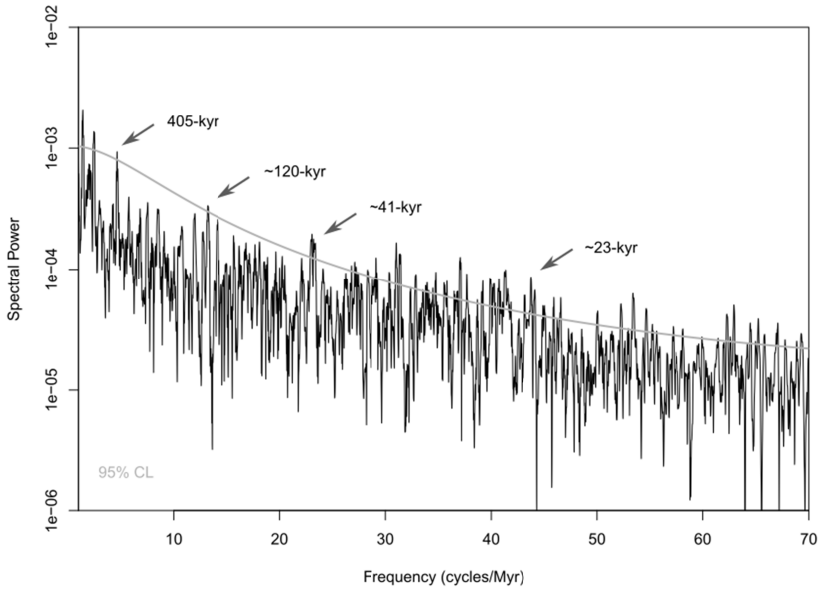

383

384 **Figure 6. Spectral power plot**. The spectral power of the paleoproductivity index and the 95%

385 confidence level (grey). Arrows point out peaks at 405-kyr, ~120-kyr, ~41-kyr and ~23-kyr.

386

387 4.2 Current winnowing

388 The Neogene portion of Site 752 is mainly foraminiferal and nannofossil oozes (Peirce &
389 Weissel, 1989). Those two sedimentary components generate a bimodal grain size distribution
390 with two distinct modes, at ~10 µm and ~150 µm, throughout the studied interval (Fig. 7b).
391 While the relative strength of these two modes are marked by considerable variability through
392 time, their position in terms of grain size is stable. This pattern indicates that calcareous
393 nannofossils and foraminifera are the two major parts of the sediments, with calcareous
394 nannofossils making up the bulk part of the finest sediment (<63µm) and foraminifera making up
395 the coarser part of the sediment (100 – 350µm).

396 We find, however, strong variations in the fine fraction proportion with respect to the
397 total sediments. These variations likely reflect periods of stronger and weaker winnowing, with
398 stronger winnowing leading to a removal of the finest fraction (House et al., 1991). Although
399 there are other factors that may have influence on the grain size, they play only a minor role here
400 over Broken Ridge (House et al., 1991). The most common among these factors is dissolution.
401 However, the paleodepths were always above the lysocline (Prell and Peterson, 1985, Rea and
402 Leinen, 1985), and foraminifera are well preserved throughout the Neogene. Moreover, there is
403 no dissolution pulse or sea-level change resemblance to the grain size record (House et al.,
404 1991). Therefore, we argue that the grain size record mainly reflects variations in current energy.
405 The grain-size variations are also registered by the core bulk density, with a strong negative
406 correlation between both (note the reversed y-axis for total counts on Fig. 7a). The total counts
407 reflect sediment bulk density, which is thus inversely correlated with grain size and current
408 winnowing intensity.

409 The total counts time-series and the percentage of the grain size >63µm series both
410 suggest a decrease in winnowing between 23 – 19.2 Ma, as well as between 15 – 13.7 Ma (Fig.
411 7a). In Figure 7b, these intervals of weakening winnowing are marked by shifts in the relative
412 importance, away from the coarser mode, towards the finer mode in the grain size distribution.
413 The 15-13.7 Ma declining trend culminates in the finest sediment grain size distribution observed
414 in the studied interval between 13.7 and 10.8 Ma (Fig. 7). There are three periods during which
415 winnowing becomes stronger and grain size distribution coarser: 19.2 – 16 Ma, 10.8– 8 Ma, and
416 ~2.6 Ma to the recent. The relative importance of the foraminifera mode increases during these
417 higher current energy intervals (Fig. 7b).

418 Current winnowing was important in the earliest Miocene portion of the record, then
419 gradually decreased until 19.2 Ma. We relate this relatively strong winnowing to Antarctic
420 Intermediate Waters (AAIW) flowing over Broken Ridge. In the earliest Miocene, two
421 intermediate water masses were present in the Indian Ocean, with Tethyan Intermediate Waters
422 (TIW) coming in from the northwest and occupying the intermediate water depth range in most
423 of the western Indian Ocean. As a consequence, AAIW was forced to spread into the eastern
424 Indian Ocean with vigorous flow over Broken Ridge (Wyrtki et al., 1971, Fine, 1993). The
425 decline in winnowing energy over Broken Ridge between 23 and 19.2 Ma coincided with the
426 initial disconnection between the Indian Ocean and the Tethys Sea due to the restriction of the
427 Mesopotamian gateway (Bialik et al., 2019). This restriction resulted in a weakening of the low-
428 latitude circumglobal ocean circulation, and TIW was gradually being cut off from its source. As
429 a consequence, AAIW had the opportunity to occupy a larger part of the intermediate water
430 depth range in the Indian Ocean, and expand to the west. In other words, AAIW could have
431 dissipated its kinetic energy over an increasingly large area, with a reduction in current

winnowing over Broken Ridge as a result. In contrast, the subsequent interval between 19.2 to 16 Ma was characterized by a marked increase in current winnowing. We attribute this increase in winnowing to an eastward shift in the AAIW flow, which would then be again more focused over Broken Ridge. As a result, Broken Ridge would have been increasingly exposed to more energetic oceanic currents. However, the driving factor that caused AAIW shift eastward remains unclear. A second decline in both winnowing proxies is observed between 15 – 13.7 Ma, which corresponds with the final closure of the Mesopotamian Seaway around 13.8 Ma (Bialik et al., 2019). This closure led to the complete termination of low-latitude circumglobal ocean circulation, and also to a further weakening of Indian Ocean circulation and a reduction in winnowing over Broken Ridge. Following this evolution, a "quiet period" is discerned between 13.7 and 10.8 Ma. The "quiet period" is marked by higher percentage of finer sediments and a more distinctive nannofossil peak (Fig. 7b). The onset of the “quiet period” at Broken Ridge somewhat surprisingly coincides with the Middle Miocene Climatic Transition (MMCT) and the establishment of the West Antarctic ice sheet (Levy et al., 2016). Those significant changes in the global climate system led to a stronger meridional temperature gradient and intensification of global ocean circulation. Our results from Broken Ridge thus suggest that the ocean’s behavior around this time was actually more heterogenous then previously considered. While most of the surface and upper intermediate water depths currents see remarkable strengthening (Eberli & Betzler, 2019), ODP Site 752 on Broken Ridge experienced relatively weak intermediate currents. We note that this interval is also very stable in terms of productivity due to a simultaneous and similarly large northward tectonic and climate-belt shift.

Winnowing increases again between 10.8 and 7.5 Ma, coinciding with the first short-lived occurrences of Tasman Leakage (Christensen et al., 2021). This body of intermediate water

455 originates from the Pacific Ocean and pass directly by Broken Ridge. Hence, it provides the
456 energy to re-enhance winnowing over Broken Ridge. After 7 Ma, Tasman Leakage no longer
457 occurs as short-lived occurrences but is permanently installed over Broken Ridge, making for
458 continuously-high winnowing between 7.5 and 3 Ma. Finally, at the Pliocene-Pleistocene
459 transition, there is another notable increase in winnowing strength. This evolution coincides with
460 the intensification of glacial-interglacial cycles and the invigoration of global ocean circulation
461 (Kleiven et al. 2022).
462

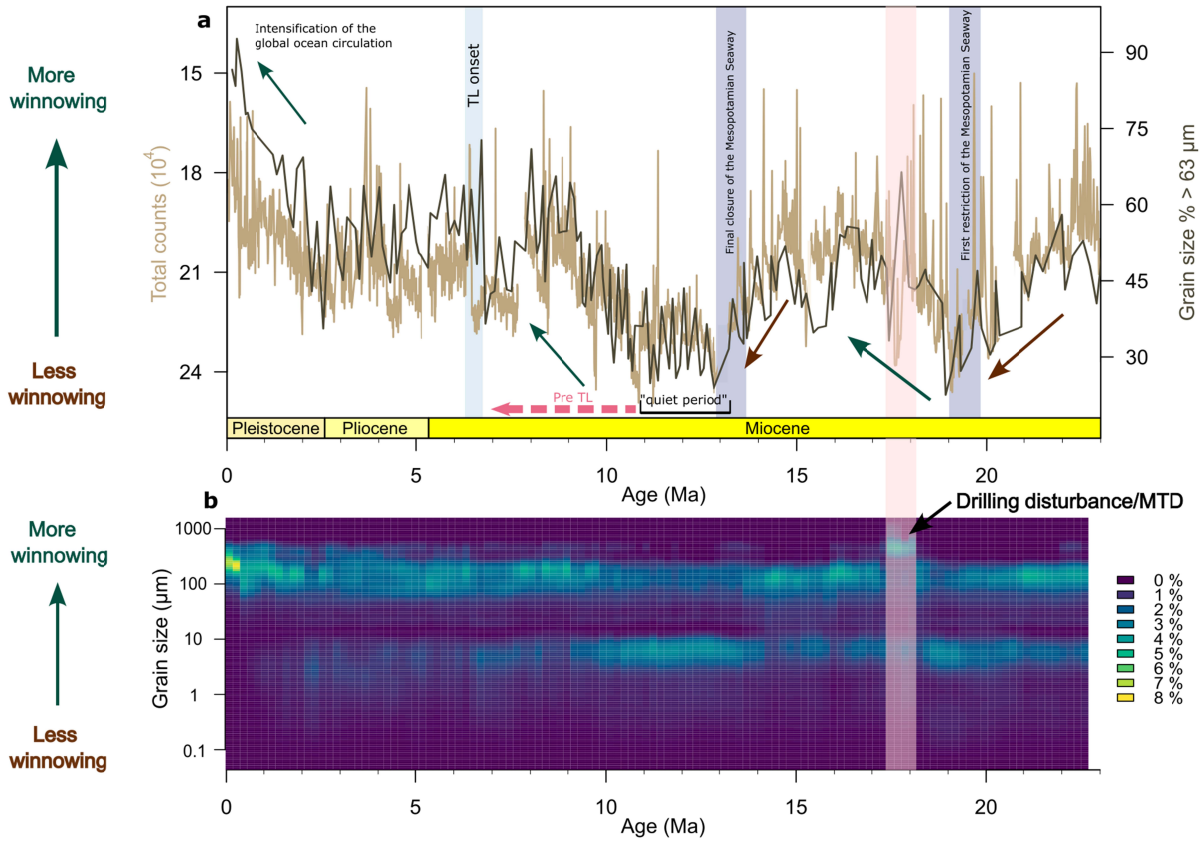

463

464 **Figure 7. Winnowing**. **(a)** Summary of all XRF-derived elements records (Total counts, beige
465 curve) and grain size record (black curve). Thick arrows mark increasing (green) and decreasing
466 (brown) of current winnowing. TL = Tasman Leakage. **(b)** grain size distribution in the

467 logarithmic scale. The black arrow point out an interval with mass transport deposit (Fig.S3).

468 MTD = Mass transport deposit.

469

4.3 Fe- and Mn-enriched dust

The presence and abundance of minerals and trace metals in Broken Ridge sediments has been used in several past studies to make inferences over global climate aridity and ocean water oxygenation (e.g., Hovan & Rea, 1991, 1992, Dickens & Owen, 1994). In the framework of this paper, we highlight that the XRF-derived Fe and Mn depth-series agree remarkably well with these previously published records (Fig. 8). The XRF-derived iron (Fe) series exhibits similar trends as the eolian component record provided in Hovan and Rea (1991, Fig. 8a), with particularly high values during the Middle Miocene and a significant decrease after ~15 Ma. While Fe counts slightly recover around 3 Ma, both proxy records remain at a low level since the Late Miocene. The manganese (Mn) time-series shows a good agreement with the data generated by Dickens & Owen (1994), which exhibits a similar evolution, with highest counts in the Early and Middle Miocene and much lower values after that. The decline of Mn (Fig. 8b) and Mn/Sc ratio in the sediment between 6.5 and 3 Ma has been described to an expansion of the OMZ by Dickens & Owen (1994). However, in the light of our winnowing reconstruction presented-above, the overall decrease in sedimentary Mn content may potentially be driven by the long-term increase in current energy.

The decline of Fe and Mn in the Early and Middle Micoene is intriguing, as simultaneously elevated Fe and Mn counts hint towards submarine hydrothermal activity and the Amsterdam – St. Paul hotspot was only ~500 km away from Broken Ridge in the Early Miocene (Janin et al., 2011, Maia et al., 2011, Resing et al., 2015). However, Hovan and Rea (1991) did not find volcanogenic materials in their investigated smear slides from ODP Hole 752A. Hence, we adhere to their original interpretation that the mineral component of Broken Ridge Neogene sediments is mostly eolian in nature, and that changes in mineral flux reflect major climatic shifts

493 in the southern African dust source. For example, Hovan and Rea (1991) interpreted the major
494 Early and Middle Miocene spikes as well as the minor peak at ~3 Ma (Fig. 8a) as indicators of
495 the aridification of the dust source region. A more elaborate analysis of mineral sediments
496 provenance and its implications is beyond the scope of this paper, and therefore, requires for
497 future research from ODP Site 752; however, we stipulate that the Neogene eolian sediments
498 over Broken Ridge was composed of an Fe- and Mn-enriched dust type.

499

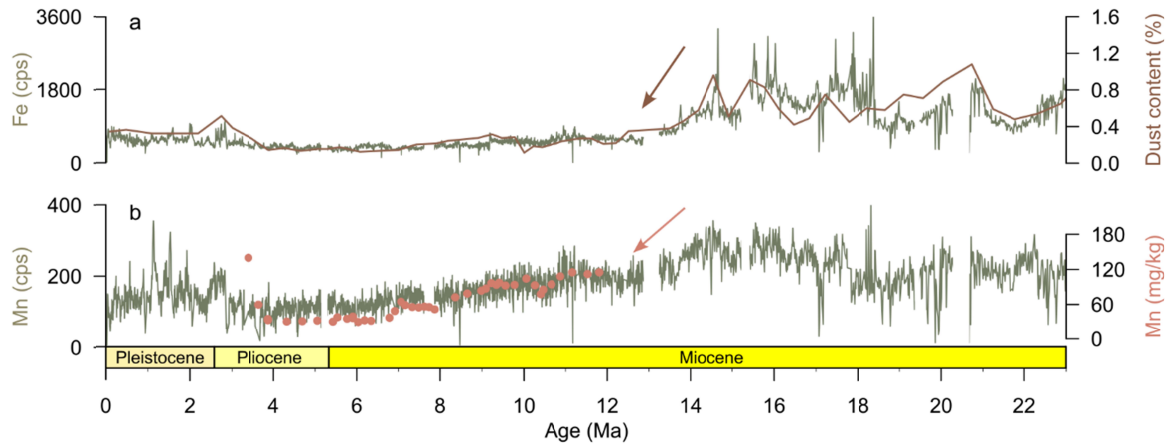

500

501 **Figure 8. Fe and Mn enriched dust. (a)** XRF-derived Fe (green) compared to the extracted dust
502 content reconstruction by Hovan & Rea (brown, Hovan & Rea, 1991); **(b)** XRF-derived Mn
503 (green) compared to Mn concentrations as measured by Dickens & Owen (light brown dots,
504 Dickens & Owen, 1994). Arrows point the significant decline in Fe and Mn after ~15 Ma.

505

506

5 Conclusions

The main patterns observed in the XRF records of ODP Hole 752A coincide with major Neogene climate evolutionary steps. The Miocene Climatic Optimum is characterized by high variability and generally high productivity index, with productivity of ODP Hole 752A pulsing at the same eccentricity beat as the dynamics of the global climate, ocean and carbon cycle. Following 13.9 Ma and the expansion of the Antarctic ice sheet, ODP Hole 752A experienced a decline in productivity and current winnowing, in conjunction with the northward shift of latitudinal climate belts and oceanographic reorganization. The productivity index stabilized at moderate levels during the Late Miocene and Pliocene. This stabilization is likely due to the combined effect of a northward tectonic movement of the site and a gradual northward shift of the climate belts. In the last 3 Myr, increased productivity and current winnowing proxies is observed. These changes are interpreted to be the result of invigorated ocean circulation at the time of intensifying northern hemisphere glaciation. The XRF-derived Fe and Mn series provide a high-resolution record, probably reflecting eolian dust, in good agreement with previous low-resolution smear-slide analyses (Hovan & Rea, 1991). These higher resolution dust records form the basis for future provenance analyses and a more detailed investigation of eolian dust fluxes. The above-described features are constrained in time by an astronomically-calibrated age-depth model. This provides a reference framework for future paleoclimatic and paleoceanographic studies.

However, to further improve the precision and accuracy of future paleoceanographic studies, particularly those focusing on Milanković (obliquity and precession) timescales, obtaining higher-resolution and fully-continuous sedimentary records is essential. This can be achieved by re-drilling Broken Ridge with state-of-the art coring techniques and strategies. This includes the

use of the advanced piston corer (APC) and the construction of a stratigraphically complete composite section by splicing (at least) three different holes at the same site.

Acknowledgments

This research used samples and data provided by the International Ocean Discovery Program (IODP) and its predecessor, the Ocean Drilling Program (ODP). We thank all scientific participants and crew of ODP Leg 121 for making this study possible. We also thank the staff of the Kochi Core Center (KCC) and the Japan-Agency for Marine-Earth Sciences and Technology (JAMSTEC) for the generous use of their facility and equipment, including the Itrax XRF-core scanner. The German Research Foundation (DFG) provided funding through Project 446900747 (VL96/3-1) awarded to DDV.

Open Research

X-Ray Fluorescence and grain size analysis data can be accessed in PANGEA (Lyu et al., 2023). The R scripts used to generate Figure 1-8 will be submitted to Zenodo as the open access resource once the manuscript is accepted. All data is temporarily available as Supporting Information.

References

Amante, C. and B.W. Eakins, 2009. ETOPO1 1 Arc-Minute Global Relief Model: Procedures, Data Sources and Analysis. NOAA Technical Memorandum NESDIS NGDC-24. National Geophysical Data Center, NOAA. https://doi.org/10.7289/V5C8276M

Bartoli, G., Sarnthein, M., Weinelt, M., Erlenkeuser, H., Garbe-Schönberg, D., & Lea, D. W. (2005). Final closure of Panama and the onset of northern hemisphere glaciation. *Earth and Planetary Science Letters, 237*(1-2), 33-44. https://doi.org/10.1016/j.epsl.2005.06.020

Berggren, W. A., Kent, D. V., Flynn, J. J., & Van Couvering, J. A. (1985). Cenozoic geochronology. *Geological Society of America Bulletin*, *96*(11), 1407. https://doi.org/10.1130/0016-7606(1985)96<1407:CG>2.0.CO;2

Betzler, C., Eberli, G. P., Kroon, D., Wright, J. D., Swart, P. K., Nath, B. N., Alvarez-Zarikian, C. A., Alonso-García, M., Bialik, O. M., Blättler, C. L., Guo, J. A., Haffen, S., Horozal, S., Inoue, M., Jovane, L., Lanci, L., Laya, J. C., Mee, A. L. H., Lüdmann, T., … Young, J. R. (2016). The abrupt onset of the modern South Asian Monsoon winds. *Scientific Reports*, *6*(1), 29838. https://doi.org/10.1038/srep29838

Bialik, O. M., Frank, M., Betzler, C., Zammit, R., & Waldmann, N. D. (2019). Two-step closure of the Miocene Indian Ocean Gateway to the Mediterranean. *Scientific Reports*, *9*(1), 8842. https://doi.org/10.1038/s41598-019-45308-7

Broeker, W. (1991), The Great Ocean Conveyor. *Oceanography*, *4*(2), 79–89, https://doi.org/10.5670/oceanog.1991.07

Christensen, B. A., De Vleeschouwer, D., Henderiks, J., Groeneveld, J., Auer, G., Drury, A. J., Karatsolis, B. T., Lyu, J., Betzler, C., Eberli, G. P., & Kroon, D. (2021). Late Miocene

571 Onset of Tasman Leakage and Southern Hemisphere Supergyre Ushers in Near-Modern
572 Circulation. *Geophysical Research Letters*, *48*(18).
573 https://doi.org/10.1029/2021GL095036
574 Clift, P. D., Betzler, C., Clemens, S. C., Christensen, B., Eberli, G. P., France-Lanord, C.,
575 Gallagher, S., Holbourn, A., Kuhnt, W., Murray, R. W., Rosenthal, Y., Tada, R., & Wan,
576 S. (2022). A synthesis of monsoon exploration in the Asian marginal seas. *Scientific*
577 *Drilling*, *31*, 1–29. https://doi.org/10.5194/sd-31-1-2022.
578 Crampton, J.S., Cody, R.D., Levy, R., Harwood, D., McKay, R. and Naish, T.R., 2016. Southern
579 Ocean phytoplankton turnover in response to stepwise Antarctic cooling over the past 15
580 million years. *Proceedings of the National Academy of Sciences, 113*(25), pp.6868-6873.
581 https://doi.org/10.1073/pnas.1600318113.
582 de Ruijter, W. P., Van Leeuwen, P. J., & Lutjeharms, J. R. (1999). Generation and evolution of
583 Natal Pulses: Solitary meanders in the Agulhas Current. *Journal of physical*
584 *oceanography*, *29*(12), 3043-3055. https://doi.org/10.1175/1520-
585 0485(1999)029<3043:GAEONP>2.0.CO;2
586 De Vleeschouwer, D., Auer, G., Smith, R., Bogus, K., Christensen, B., Groeneveld, J., ... &
587 Pälike, H. (2018). The amplifying effect of Indonesian Throughflow heat transport on
588 Late Pliocene Southern Hemisphere climate cooling. *Earth and Planetary Science Letters*,
589 *500*, 15-27. https://doi.org/10.1016/j.epsl.2018.07.035
590 De Vleeschouwer, D., Drury, A. J., Vahlenkamp, M., Rochholz, F., Liebrand, D., & Pälike, H.
591 (2020). High-latitude biomes and rock weathering mediate climate–carbon cycle
592 feedbacks on eccentricity timescales. *Nature Communications*, *11*(1), 5013.
593 https://doi.org/10.1038/s41467-020-18733-w.

De Vleeschouwer, D., Peral, M., Marchegiano, M., Füllberg, A., Meinicke, N., Pälike, H., ... & Claeys, P. (2022). Plio-Pleistocene Perth Basin water temperatures and Leeuwin Current dynamics (Indian Ocean) derived from oxygen and clumped-isotope paleothermometry. *Climate of the Past*, *18*(5), 1231-1253. https://doi.org/10.5194/cp-18-1231-2022.

De Vleeschouwer, D., Vahlenkamp, M., Crucifix, M., & Pälike, H. (2017). Alternating Southern and Northern Hemisphere climate response to astronomical forcing during the past 35 my. *Geology*, *45*(4), 375-378. https://doi.org/10.1130/G38663.1.

Demenocal, P. B. (1995). Plio-pleistocene African climate. *Science*, *270*(5233), 53-59. https://doi.org/10.1126/science.270.5233.53

Dickens, G. R., & Owen, R. M. (1994). Late Miocene-Early Pliocene manganese redirection in the central Indian Ocean: Expansion of the Intermediate Water oxygen minimum zone. *Paleoceanography*, *9*(1), 169–181. https://doi.org/10.1029/93PA02699

Dickens, G. R., & Owen, R. M. (1999). The latest Miocene–early Pliocene biogenic bloom: a revised Indian Ocean perspective. *Marine Geology*, *161*(1), 75-91. https://doi.org/10.1016/S0025-3227(99)00057-2.

Dodson, J. R., & Macphail, M. K. (2004). Palynological evidence for aridity events and vegetation change during the Middle Pliocene, a warm period in Southwestern Australia. *Global and Planetary Change*, *41*(3-4), 285-307. https://doi.org/10.1016/j.gloplacha.2004.01.013

Driscoll, N.W., and Karner, G.D., 1991. Deconvolving water-gun seismic data. In Weissel, J., Peirce, J., Taylor, E., Alt, J., et al., *Proc. ODP, Sci. Results, 121*: College Station, TX (Ocean Drilling Program), 663–679. https://doi.org/10.2973/odp.proc.sr.121.156.1991.

616 Duesing, W., Kaboth-Bahr, S., Asrat, A., Cohen, A. S., Foerster, V., Lamb, H. F., ... & Viehberg,
617 F. (2021). Changes in the cyclicity and variability of the eastern African paleoclimate
618 over the last 620 kyrs. *Quaternary Science Reviews, 273*, 107219.
619 https://doi.org/10.1016/j.quascirev.2021.107219
620 Dupont, L. M. (2006). Late Pliocene vegetation and climate in Namibia (southern Africa)
621 derived from palynology of ODP Site 1082. *Geochemistry, Geophysics, Geosystems*, *7*(5).
622 https://doi.org/10.1029/2005GC001208
623 Durgadoo, J. V., Rühs, S., Biastoch, A., & Böning, C. W. B. (2017). Indian Ocean sources of
624 Agulhas leakage: INDIAN OCEAN SOURCES OF AGULHAS LEAKAGE. *Journal of*
625 *Geophysical Research: Oceans*, *122*(4), 3481–3499.
626 https://doi.org/10.1002/2016JC012676
627 Eberli, G. P., & Betzler, C. (2019). Characteristics of modern carbonate contourite drifts.
628 *Sedimentology*, *66*(4), 1163-1191. https://doi.org/10.1111/sed.12584
629 Farrell, J. W., Raffi, I., Janecek, T. R., Murray, D. W., Levitan, M., Dadey, K. A., ... & Hovan11,
630 S. (1995). 35. LATE NEOGENE SEDIMENTATION PATTERNS IN THE EASTERN
631 EQUATORIAL PACIFIC OCEAN1. In Proceedings of the ocean drilling program,
632 scientific results (Vol. 138).
633 Fine, Rana A. (1993). Circulation of Antarctic intermediate water in the South Indian Ocean.
634 *Deep Sea Research Part I: Oceanographic Research Papers 40*.10: 2021-2042.
635 https://doi.org/10.1016/0967-0637(93)90043-3
636 Fitzsimmons, J. N., John, S. G., Marsay, C. M., Hoffman, C. L., Nicholas, S. L., Toner, B. M., ...
637 & Sherrell, R. M. (2017). Iron persistence in a distal hydrothermal plume supported by

638 dissolved–particulate exchange. *Nature Geoscience*, *10*(3), 195-201. https://doi.org/
639 10.1038/NGEO2900.
640 Fujioka, T., Chappell, J., Fifield, L. K., & Rhodes, E. J. (2009). Australian desert dune fields
641 initiated with Pliocene–Pleistocene global climatic shift. *Geology*, *37*(1), 51-54.
642 https://doi.org/10.1130/G25042A.1
643 German, C. R., & Von Damm, K. L. (2006). Hydrothermal processes. *Treatise on geochemistry*,
644 *6*, 181-222.
645 Grant, K.M. and Dickens, G.R., 2002. Coupled productivity and carbon isotope records in the
646 southwest Pacific Ocean during the late Miocene–early Pliocene biogenic bloom.
647 *Palaeogeography, Palaeoclimatology, Palaeoecology, 187*(1-2), pp.61-82.
648 https://doi.org/10.1016/S0031-0182(02)00508-4
649 Groeneveld, J., Henderiks, J., Renema, W., McHugh, C. M., De Vleeschouwer, D., Christensen,
650 B. A., ... & Expedition 356 Scientists. (2017). Australian shelf sediments reveal shifts in
651 Miocene Southern Hemisphere westerlies. *Science Advances*, *3*(5), e1602567.
652 https://doi.org/10.1126/sciadv.1602567.
653 Gordon, A. L. (2003). The brawniest retroflection. *Nature*, *421*(6926), 904–905.
654 https://doi.org/10.1038/421904a
655 Gordon, A. L. (2005). Oceanography of the Indonesian seas and their throughflow.
656 Oceanography, *18*(4), 14-27. https://doi:10.5670/oceanog.2005.18.
657 Gupta, A. K., Singh, R. K., & Verma, S. (2013). Deep-sea palaeoceanographic evolution of the
658 eastern Indian Ocean during the late Oligocene–Pleistocene: species diversity trends in
659 benthic foraminifera. *Current Science*, *104* (7), 904-910.
660 https://www.jstor.org/stable/24092103

Haq, B. U., Hardenbol, J., & Vail, P. R. (1987). Chronology of Fluctuating Sea Levels Since the Triassic. *Science*, *235*(4793), 1156–1167. https://doi.org/10.1126/science.235.4793.1156

Herbert, T. D., Lawrence, K. T., Tzanova, A., Peterson, L. C., Caballero-Gill, R., & Kelly, C. S. (2016). Late Miocene global cooling and the rise of modern ecosystems. *Nature Geoscience*, *9*(11), 843–847. https://doi.org/10.1038/ngeo2813.

Hermoyian, C.S. and Owen, R.M., 2001. Late Miocene-early Pliocene biogenic bloom: Evidence from low-productivity regions of the Indian and Atlantic Oceans. *Paleoceanography, 16*(1), pp.95-100. https://doi.org/10.1029/2000PA000501.

Holbourn, A., Kuhnt, W., Kochhann, K. G., Andersen, N., & Sebastian Meier, K. J. (2015). Global perturbation of the carbon cycle at the onset of the Miocene Climatic Optimum. *Geology, 43*(2), 123-126. https://doi.org/10.1130/G36317.1

Holbourn, A., Kuhnt, W., Schulz, M., Flores, J. A., & Andersen, N. (2007). Orbitally-paced climate evolution during the middle Miocene "Monterey" carbon-isotope excursion. *Earth and Planetary Science Letters, 261*(3-4), 534-550. https://doi.org/10.1016/j.epsl.2007.07.026.

House, M. A., Rea, D. K., & Janecek, T. R. (1991). Grain-size record of ocean current winnowing in Oligocene to Pleistocene ooze, Broken Ridge, southeastern Indian Ocean. *In* Peirce, J., Weissel, J., et al., *Proc. ODP, Init. Repts., 121*: College Station, TX (Ocean Drilling Program), 507–516. https://doi.org/10.2973/odp.proc.ir.121.114.1989.

Hovan, S.A., and Rea, D.K., (1991). Post-Eocene record of eolian deposition at Sites 752, 754, and 756. *In* Weissel, J., Peirce, J., Taylor, E., Alt, J., et al., *Proc. ODP, Sci. Results, 121*: College Station, TX (Ocean Drilling Program), 219–228. https://doi.org/10.2973/odp.proc.sr.121.125.1991

Hovan, Steven A., and David K. Rea. (1992). "The Cenozoic record of continental mineral deposition on Broken and Ninetyeast Ridges, Indian Ocean: southern African aridity and sediment delivery from the Himalayas." *Paleoceanography 7*(6), 833-860. https://doi.org/10.1029/92PA02176

Janin, M., HÉmond, C., Guillou, H., Maia, M., Johnson, K. T. M., Bollinger, C., ... & Mudholkar, A. (2011). Hot spot activity and tectonic settings near Amsterdam–St. Paul plateau (Indian Ocean). *Journal of Geophysical Research: Solid Earth, 116*(B5). https://doi.org/10.1029/2010JB007800

Karatsolis, B. T., Lougheed, B. C., De Vleeschouwer, D., & Henderiks, J. (2022). Abrupt conclusion of the late Miocene-early Pliocene biogenic bloom at 4.6-4.4 Ma. *Nature Communications*, *13*(1), 353. https://doi.org/10.1038/s41467-021-27784-6.

Kassambara, A., & Mundt, F. (2017). Package 'factoextra'. Extract and visualize the results of multivariate data analyses, 76(2). https://doi.org/10.1029/92PA02176

Kleiven, H. F., Jansen, E., Fronval, T., & Smith, T. M. (2002). Intensification of Northern Hemisphere glaciations in the circum Atlantic region (3.5–2.4 Ma)–ice-rafted detritus evidence. *Palaeogeography, Palaeoclimatology, Palaeoecology*, *184*(3-4), 213-223. https://doi.org/10.1016/S0031-0182(01)00407-2

Krebs, U., Park, W., & Schneider, B. (2011). Pliocene aridification of Australia caused by tectonically induced weakening of the Indonesian throughflow. *Palaeogeography, Palaeoclimatology, Palaeoecology*, *309*(1-2), 111-117. https://doi.org/10.1016/j.palaeo.2011.06.002

Kuhnt, W., Holbourn, A., Hall, R., Zuvela, M., & Käse, R. (2004). Neogene history of the Indonesian Throughflow. In P. Clift, W. Kuhnt, P. Wang, & D. Hayes (Eds.),

Geophysical Monograph Series (Vol. 149, pp. 299–320). American Geophysical Union. https://doi.org/10.1029/149GM16.

Levy, R., Harwood, D., Florindo, F., Sangiorgi, F., Tripati, R., von Eynatten, H., Gasson, E., Kuhn, G., Tripati, A., DeConto, R. and Fielding, C., 2016. Antarctic ice sheet sensitivity to atmospheric CO2 variations in the early to mid-Miocene. *Proceedings of the National Academy of Sciences, 113*(13), pp.3453-3458. https://doi.org/10.1073/pnas.1516030113.

Liu, C., Nie, J., Li, Z., Qiao, Q., Abell, J. T., Wang, F., & Xiao, W. (2021). Eccentricity forcing of East Asian monsoonal systems over the past 3 million years. *Proceedings of the National Academy of Sciences, 118*(43), e2107055118. https://doi.org/10.1073/pnas.2107055118

Löwemark, L., Bloemsma, M., Croudace, I., Daly, J. S., Edwards, R. J., Francus, P., ... & Turner, J. N. (2019). Practical guidelines and recent advances in the Itrax XRF core-scanning procedure. *Quaternary International*, *514*, 16-29. https://doi.org/10.1016/j.quaint.2018.10.044

Lyle, M., Dadey, K. A., & Farrell, J. W. (1995). The Late Miocene (11-8 Ma) Eastern Pacific Carbonate Crash: evidence for reorganization ofdeep-water Circulation by the closure of the Panama Gateway. In N. G. Pisias, L. A. Mayer, T. R. Janecek, A. Palmer-Julson & T. H. vanAndel (Eds.), *Proceedings of the Ocean Drilling Program* (Vol. 138, pp. 821–838). College Station, TX: Ocean Drilling Program. https://doi.org/10.2973/odp.proc.sr.138.157.1995

Lyu, Jing; Auer, Gerald; Bialik, Or M; Christensen, Beth A; Yamaoka, Ryo; De Vleeschouwer, David: (2023) Raw X-ray fluorescence (XRF) scanning and grain size analysis of ODP

729 Hole 121-752A at Broken Ridge. [Dataset]. PANGAEA,
730 https://doi.org/10.1594/PANGAEA.961153
731 Lübbers, J., Kuhnt, W., Holbourn, A. E., Bolton, C. T., Gray, E., Usui, Y., ... & Andersen, N.
732 (2019). The middle to late Miocene "Carbonate Crash" in the equatorial Indian Ocean.
733 *Paleoceanography and Paleoclimatology*, 34(5), 813-832.
734 https://doi.org/10.1029/2018PA003482.
735 Maia, M., Pessanha, I., Courrèges, E., Patriat, M., Gente, P., Hémond, C., ... & Vatteville, J.
736 (2011). Building of the Amsterdam-Saint Paul plateau: A 10 Myr history of a ridge-hot
737 spot interaction and variations in the strength of the hot spot source. *Journal of*
738 *Geophysical Research: Solid Earth, 116*(B9). https://doi.org/10.1029/2010JB007800
739 Maslin, M. A., Haug, G. H., Sarnthein, M., & Tiedemann, R. (1996). The progressive
740 intensification of northern hemisphere glaciation as seen from the North Pacific.
741 *Geologische Rundschau, 85*, 452-465. https://doi.org/10.1007/BF02369002
742 Meyers, S. R. (2012). Seeing red in cyclic stratigraphy: Spectral noise estimation for
743 astrochronology: SEEING RED IN CYCLIC STRATIGRAPHY. *Paleoceanography*,
744 *27*(3), n/a-n/a. https://doi.org/10.1029/2012PA002307
745 Meyers, S.R. (2014). Astrochron: An R Package for Astrochronology. https://cran.r-
746 project.org/package=astrochron
747 Middleton, J. F. (2002). A northern boundary current along Australia's southern shelves: The
748 Flinders Current. *Journal of Geophysical Research*, *107*(C9), 3129.
749 https://doi.org/10.1029/2000JC000701
750 Miller, K. G., Browning, J. V., Aubry, M.-P., Wade, B. S., Katz, M. E., Kulpecz, A. A., &
751 Wright, J. D. (2008). Eocene-Oligocene global climate and sea-level changes: St.

752 Stephens Quarry, Alabama. *Geological Society of America Bulletin*, *120*(1–2), 34–53.
753 https://doi.org/10.1130/B26105.1
754 Mutter, J. C., & Cande, S. C. (1983). The early opening between Broken Ridge and Kerguelen
755 Plateau. *Earth and Planetary Science Letters*, *65*(2), 369–376.
756 https://doi.org/10.1016/0012-821X(83)90174-7
757 Ohishi, S., Tozuka, T., & Cronin, M. F. (2017). Frontogenesis in the Agulhas Return Current
758 Region Simulated by a High-Resolution CGCM. *Journal of Physical Oceanography*,
759 *47*(11), 2691–2710. https://doi.org/10.1175/JPO-D-17-0038.1.
760 Pillot, Q., Suchéras-Marx, B., Sarr, A.C., Bolton, C.T. and Donnadieu, Y., 2023. A global
761 reassessment of the spatial and temporal expression of the Late Miocene Biogenic Bloom.
762 *Paleoceanography and Paleoclimatology*, p.e2022PA004564.
763 https://doi.org/10.1029/2022PA004564
764 Pospichal, J.J., Dehn, J., Driscoll, N.W., van Eijden, A.J.M., Farrell, J.W., Fourtanier, E.,
765 Gamson, P., Gee, J., Janecek, T.R., Jenkins, D.G., Klootwijk, C., Nomura, R., Owen,
766 R.M., Rea, D.K., Resiwati, P., Smit, J., and Smith, G., 1991. Cretaceous–Paleogene
767 biomagnetostratigraphy of Sites 752–755, Broken Ridge: a synthesis. *In* Weissel, J.,
768 Peirce, J., Taylor, E., Alt, J., et al., *Proc. ODP, Sci. Results, 121*: College Station, TX
769 (Ocean Drilling Program), 721–741. https://doi.org/10.2973/odp.proc.sr.121.181.1991
770 Raffi, I., Wade, B.S., Pälike, H., Beu, A.G., Cooper, R., Crundwell, M.P., Krijgsman, W., Moore,
771 T., Raine, I., Sardella, R., Vernyhorova, Y.V. (2020). Chapter 29 - The Neogene Period,
772 Editor(s): Felix M. Gradstein, James G. Ogg, Mark D. Schmitz, Gabi M. Ogg, Geologic
773 Time Scale 2020*, Elsevier*. https://doi.org/10.1016/B978-0-12-824360-2.00029-2.

774 Ridgway, K. R., & Dunn, J. R. (2007). Observational evidence for a Southern Hemisphere
775 oceanic supergyre: SOUTHERN HEMISPHERE OCEANIC SUPERGYRE. Geophysical
776 Research Letters, 34(13), n/a-n/a. https://doi.org/10.1029/2007GL030392
777 Resing, J. A., Sedwick, P. N., German, C. R., Jenkins, W. J., Moffett, J. W., Sohst, B. M., &
778 Tagliabue, A. (2015). Basin-scale transport of hydrothermal dissolved metals across the
779 South Pacific Ocean. *Nature, 523*(7559), 200-203. https://doi.org/10.1038/nature14577
780 Rosell-Fieschi, M., Rintoul, S. R., Gourrion, J., & Pelegrí, J. L. (2013). Tasman Leakage of
781 intermediate waters as inferred from Argo floats: TASMAN LEAKAGE FROM ARGO
782 FLOATS. *Geophysical Research Letters*, *40*(20), 5456–5460.
783 https://doi.org/10.1002/2013GL057797
784 Sclater, J. G., Meinke, L., Bennett, A., & Murphy, C. (1985). The depth of the ocean through the
785 Neogene. *Geological Society of America Memoirs, 163*, 1-20.
786 Shipboard Scientific Party, 1989. Site 752. *In* Peirce, J., Weissel, J., et al., *Proc. ODP, Init.*
787 *Repts., 121*: College Station, TX (Ocean Drilling Program), 111–169.
788 Speich, S., Blanke, B., & Madec, G. (2001). Warm and cold water routes of an OGCM
789 thermohaline conveyor belt. *Geophysical Research Letters, 28*(2), 311-314.
790 https://doi.org/10.1029/2000GL011748
791 Speich, S., Blanke, B., de Vries, P., Drijfhout, S., Döös, K., Ganachaud, A., & Marsh, R. (2002).
792 Tasman leakage: A new route in the global ocean conveyor belt: TASMAN LEAKAGE.
793 *Geophysical Research Letters*, *29*(10), 55-1-55–4.
794 https://doi.org/10.1029/2001GL014586.

795 Steiner, Z., Lazar, B., Torfstein, A. and Erez, J., 2017. Testing the utility of geochemical proxies
796 for paleoproductivity in oxic sedimentary marine settings of the Gulf of Aqaba, Red Sea.
797 *Chemical Geology, 473*, pp.40-49. https://doi.org/10.1016/j.chemgeo.2017.10.012.
798 Stocker, Thomas F., Lawrence A. Mysak, and Daniel G. Wright. (1992). "A zonally averaged,
799 coupled ocean-atmosphere model for paleoclimate studies." *Journal of Climate 5.8*: 773-
800 797. https://doi.org/10.1175/1520-0442(1992)005<0773:AZACOA>2.0.CO;2
801 Thomson, D. J. (1982). Spectrum estimation and harmonic analysis. *Proceedings of the IEEE*,
802 *70*(9), 1055–1096. https://doi.org/10.1109/PROC.1982.12433
803 Tribovillard, N., Algeo, T. J., Lyons, T., & Riboulleau, A. (2006). Trace metals as paleoredox
804 and paleoproductivity proxies: an update. *Chemical geology, 232*(1-2), 12-32.
805 https://doi.org/10.1016/j.chemgeo.2006.02.012
806 van Sebille, E., England, M. H., Zika, J. D., & Sloyan, B. M. (2012). Tasman leakage in a fine-
807 resolution ocean model: TASMAN LEAKAGE. *Geophysical Research Letters*, *39*(6),
808 n/a-n/a. https://doi.org/10.1029/2012GL051004
809 van Sebille, E., Sprintall, J., Schwarzkopf, F. U., Sen Gupta, A., Santoso, A., England, M. H.,
810 Biastoch, A., & Böning, C. W. (2014). Pacific-to-Indian Ocean connectivity: Tasman
811 leakage, Indonesian Throughflow, and the role of ENSO. *Journal of Geophysical*
812 *Research: Oceans*, *119*(2), 1365–1382. https://doi.org/10.1002/2013JC009525
813 Vervoort, P., Kirtland Turner, S., Rochholz, F., & Ridgwell, A. (2021). Earth System Model
814 Analysis of How Astronomical Forcing Is Imprinted Onto the Marine Geological Record:
815 The Role of the Inorganic (Carbonate) Carbon Cycle and Feedbacks. *Paleoceanography*
816 *and Paleoclimatology*, *36*(10). https://doi.org/10.1029/2020PA004090

817 Vail, P. R., Mitchum Jr, R. M., & Thompson III, S. (1977). Seismic stratigraphy and global
818 changes of sea level: Part 3. Relative changes of sea level from Coastal Onlap: section 2.
819 Application of seismic reflection Configuration to Stratigrapic Interpretation.
820 Wyrtki, Klaus, Edward B. Bennett, and David J. Rochford. Oceanographic atlas of the
821 international Indian Ocean expedition. Vol. 531. Washington, DC: National Science
822 Foundation, 1971.
823
824
825

Figure 1.

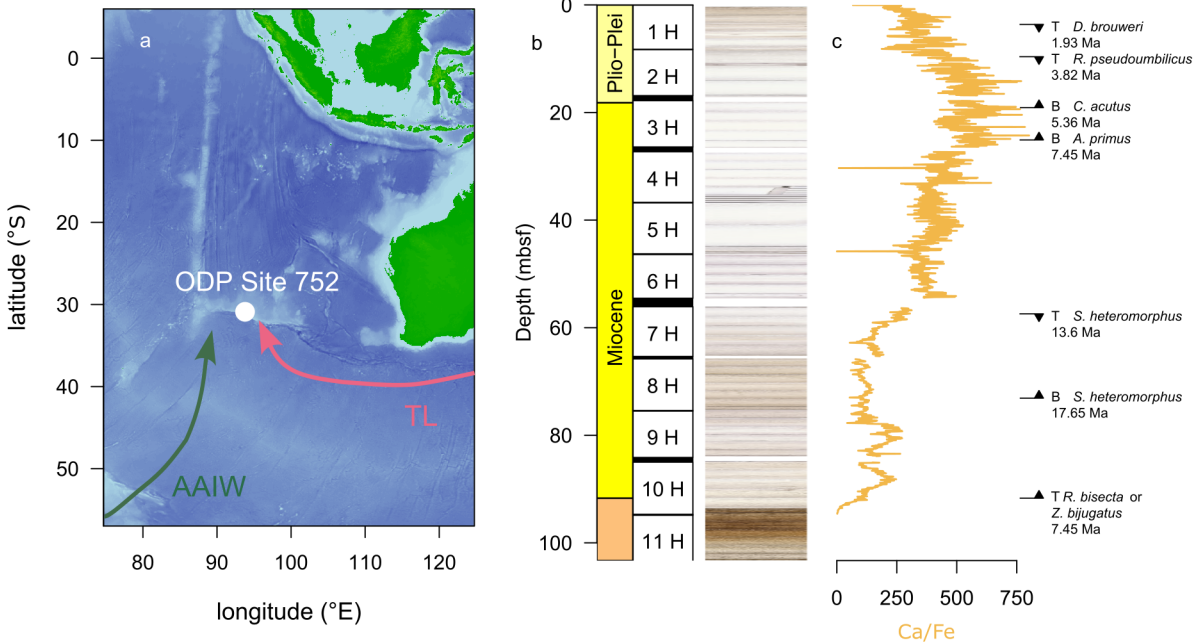
a
ODP Site 752
AAIW
TL
latitude (°S)
longitude (°E)
0
10
20
30
40
50
80
90
100
110
120
b
ODP Hole 752A
Depth (mbsf)
Plio–Plei
Miocene
1 H
2 H
3 H
4 H
5 H
6 H
7 H
8 H
9 H
10 H
11 H
c
T D. brouweri
1.93 Ma
T R. pseudoumbilicus
3.82 Ma
B C. acutus
5.36 Ma
B A. primus
7.45 Ma
T S. heteromorphus
13.6 Ma
B S. heteromorphus
17.65 Ma
T R. bisecta or
Z. bijugatus
7.45 Ma
0
250
500
750
Ca/Fe

Figure 2.

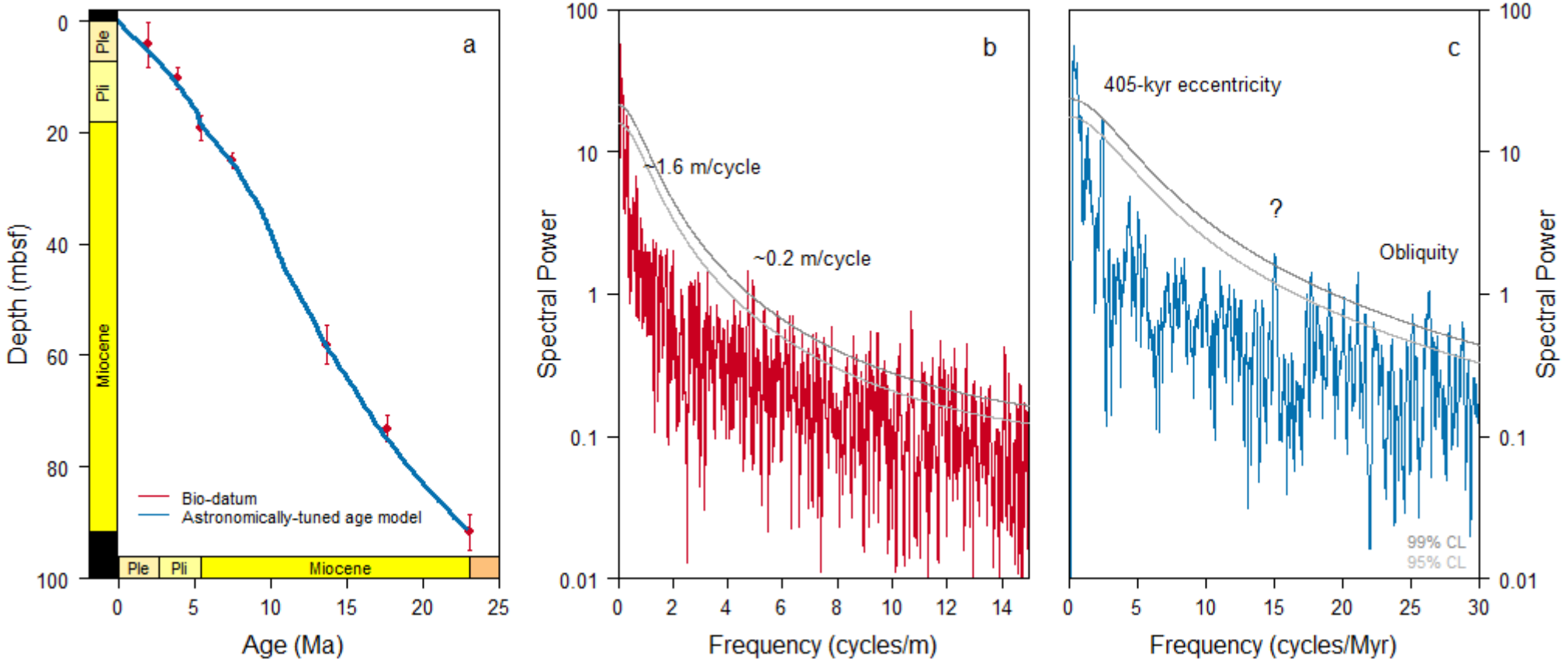
a
Depth (mbsf)
Age (Ma)
Ple
Pli
Miocene
Bio-datum
Astronomically-tuned age model
b
Spectral Power
Frequency (cycles/m)
~1.6 m/cycle
~0.2 m/cycle
c
405-kyr eccentricity
?
Obliquity
99% CL
95% CL
Frequency (cycles/Myr)

Figure 3.

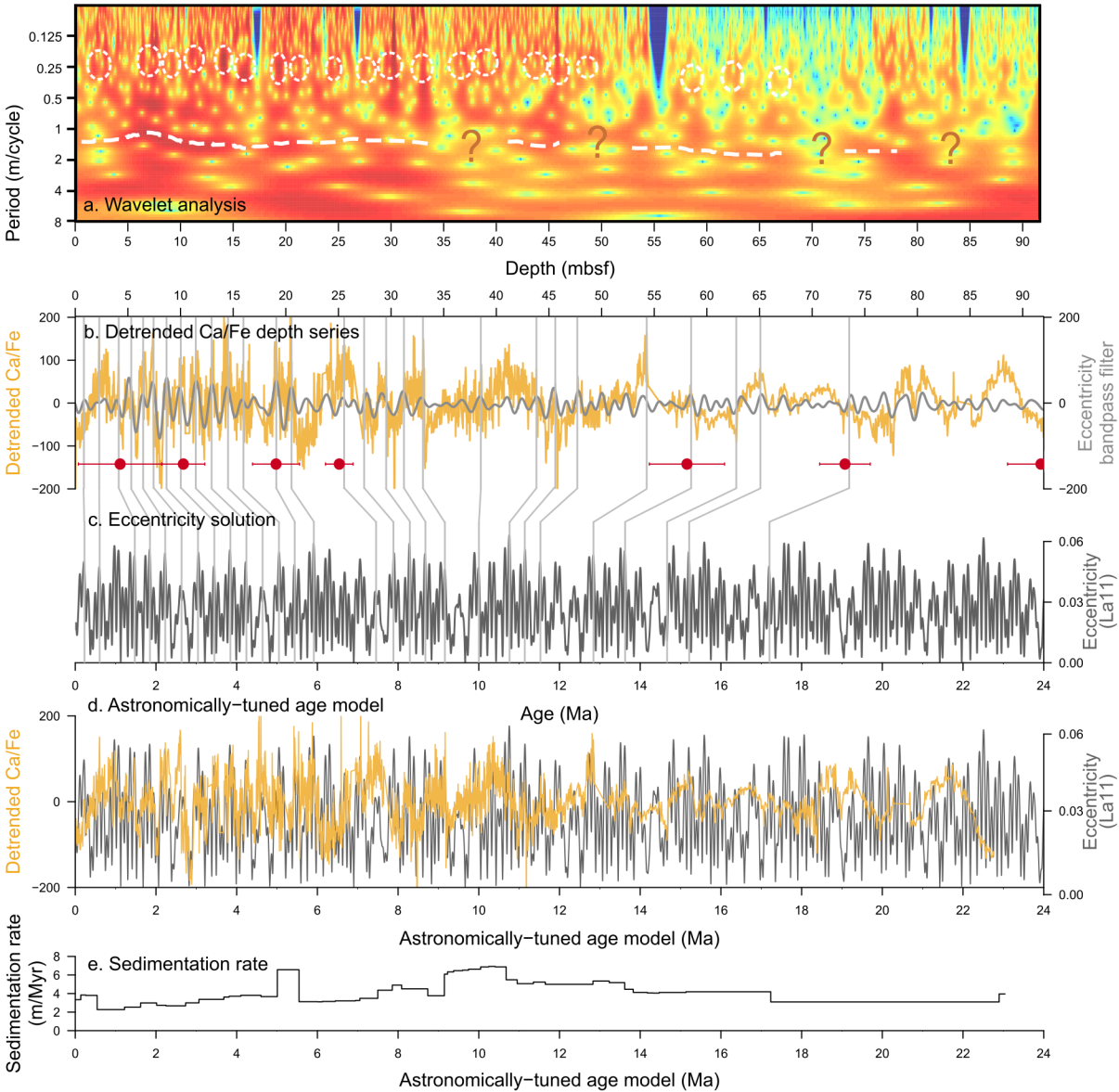
a. Wavelet analysis
Period (m/cycle)
0.125
0.25
0.5
1
2
4
8
Depth (mbsf)
b. Detrended Ca/Fe depth series
Detrended Ca/Fe
Eccentricity bandpass filter
c. Eccentricity solution
Eccentricity (La11)
d. Astronomically−tuned age model
Age (Ma)
Astronomically−tuned age model (Ma)
e. Sedimentation rate
Sedimentation rate (m/Myr)

Figure 4.

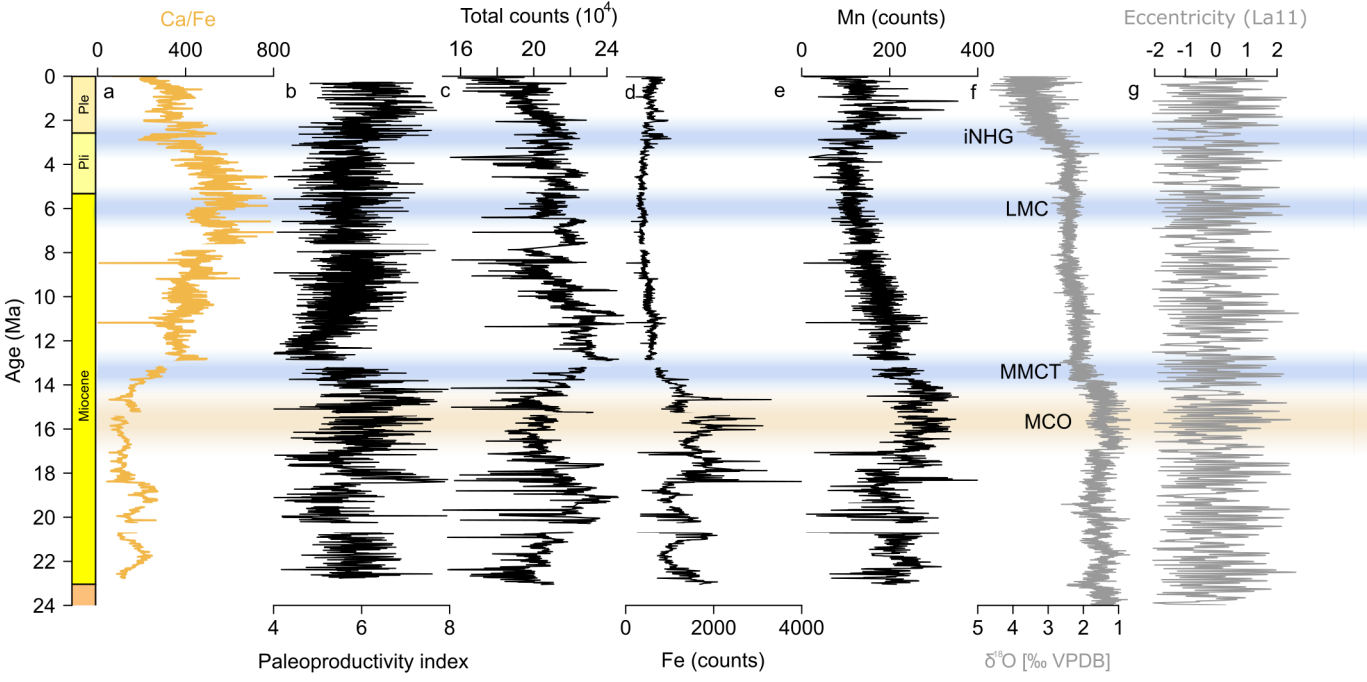
Ca/Fe
0
400
800
a
Total counts (10^4)
16
20
24
b
c
Mn (counts)
0
200
400
d
e
Eccentricity (La11)
-2
-1
0
1
2
f
g
Age (Ma)
0
2
4
6
8
10
12
14
16
18
20
22
24
Ple
Pli
Miocene
iNHG
LMC
MMCT
MCO
4
6
8
Paleoproductivity index
0
2000
4000
Fe (counts)
5
4
3
2
1
δ18O [‰ VPDB]

Figure 5.

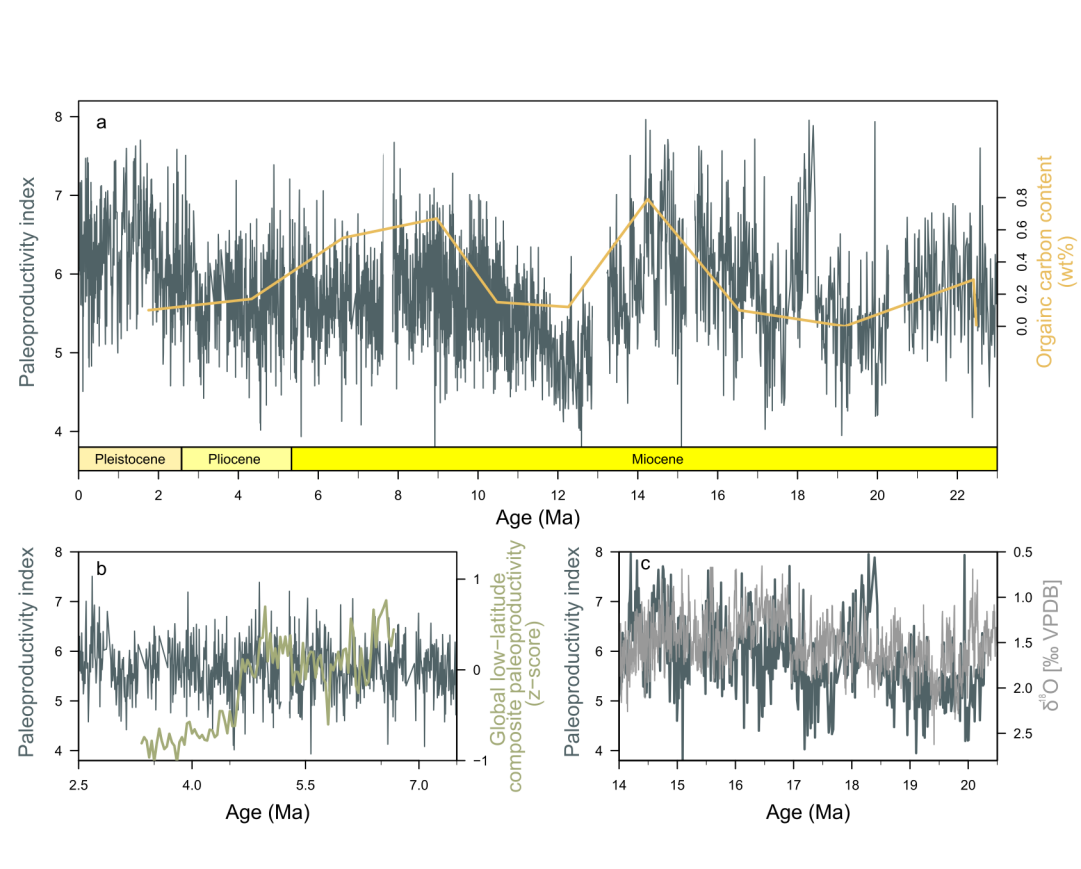
a
Paleoproductivity index
Orgainc carbon content (wt%)
Pleistocene
Pliocene
Miocene
Age (Ma)
b
Paleoproductivity index
Global low−latitude composite paleoproductivity (z−score)
Age (Ma)
c
Paleoproductivity index
δ18O [‰ VPDB]
Age (Ma)

Figure 6.

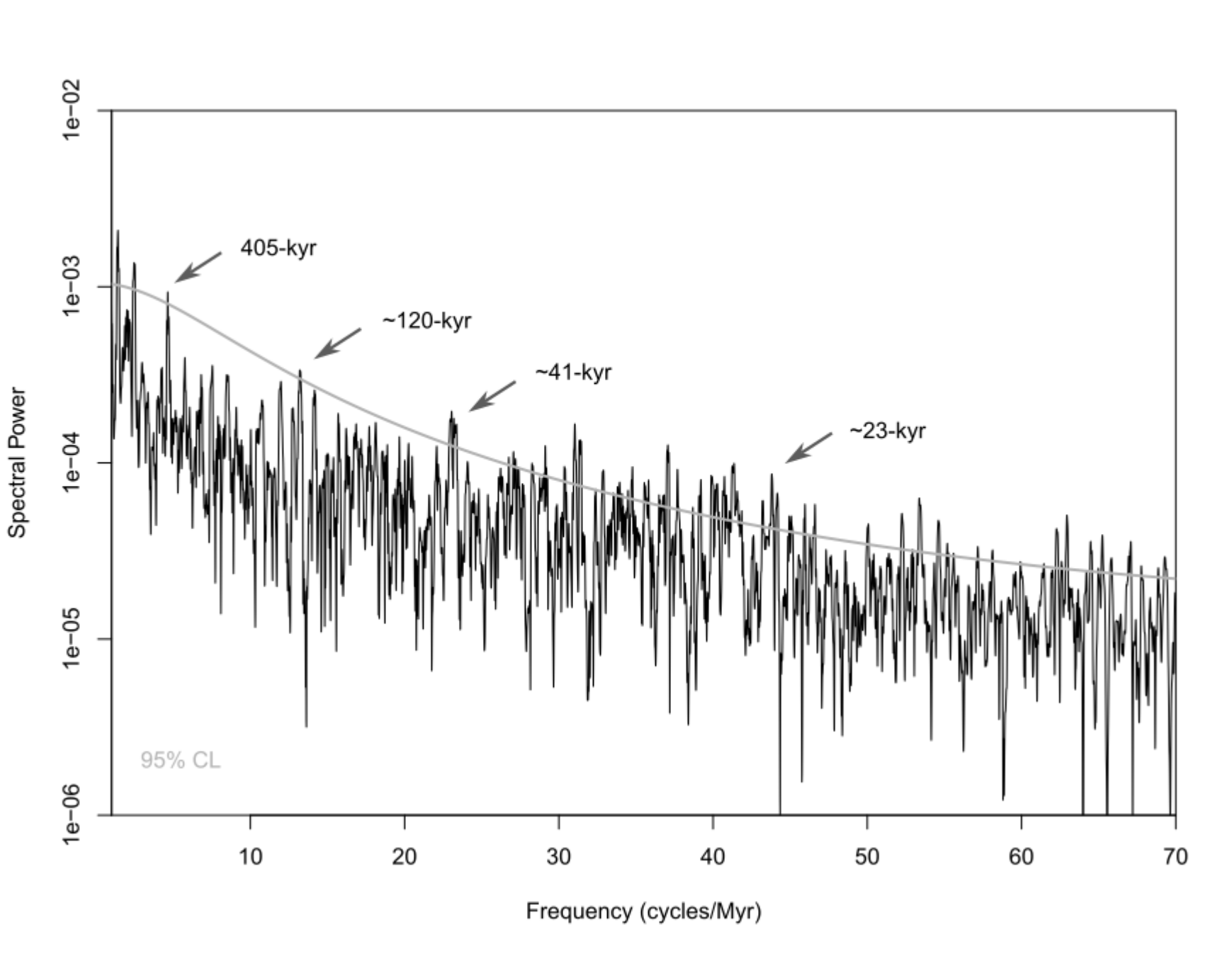
405-kyr
~120-kyr
~41-kyr
~23-kyr
95% CL
Spectral Power
1e−02
1e−03
1e−04
1e−05
1e−06
10
20
30
40
50
60
70
Frequency (cycles/Myr)

Figure 7.

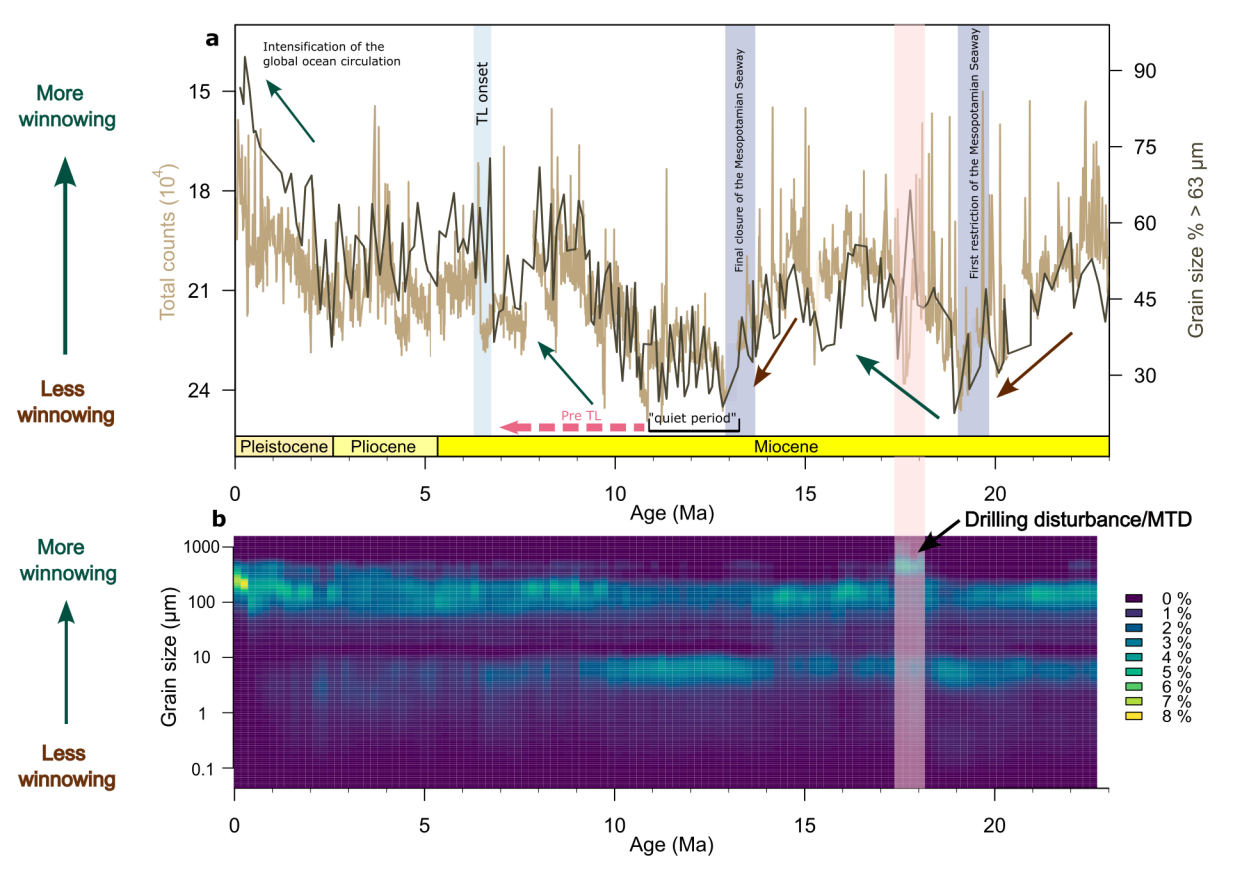
a
Intensification of the global ocean circulation
TL onset
Final closure of the Mesopotamian Seaway
First restriction of the Mesopotamian Seaway
Pre TL
"quiet period"
Pleistocene
Pliocene
Miocene
Total counts (10^4)
Grain size % > 63 µm
Age (Ma)
More winnowing
Less winnowing
b
Drilling disturbance/MTD
Grain size (µm)
0 %
1 %
2 %
3 %
4 %
5 %
6 %
7 %
8 %
Age (Ma)
More winnowing
Less winnowing

Figure 8.

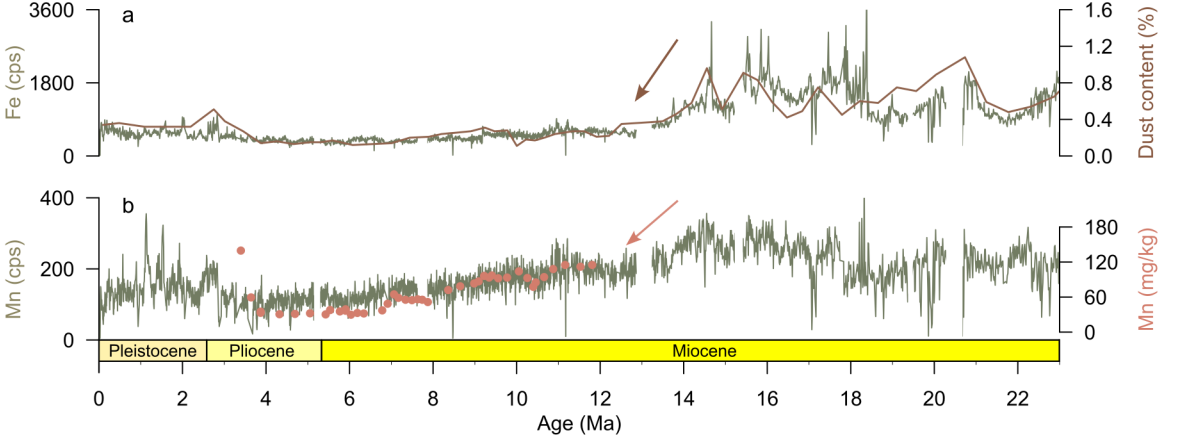
a
b
Fe (cps)
3600
1800
0
Dust content (%)
1.6
1.2
0.8
0.4
0.0
Mn (cps)
400
200
0
Mn (mg/kg)
180
120
60
0
Pleistocene
Pliocene
Miocene
0
2
4
6
8
10
12
14
16
18
20
22
Age (Ma)